The Astronomical Journal, 168:280 (18pp), 2024 December https://doi.org/10.3847/1538-3881/ad8913

KIC 6362386: An Eclipsing Binary with γ Doradus–type Pulsations and Starspots

Mengqi Jin[1,2], Jianning Fu[1,2], Xiaobin Zhang[3], Weikai Zong[1,2], Jiaxin Wang[4], Xiaoyu Ma[1,5], Keyu Xing[1], and Haotian Wang[1]
[1] Department of Astronomy, Beijing Normal University, No. 19, XinJieKouWai Street, Beijing 100875, People's Republic of China
[2] Institute for Frontiers in Astronomy and Astrophysics, Beijing Normal University, Beijing 102206, People's Republic of China
[3] Key Laboratory of Optical Astronomy, National Astronomical Observatories, Chinese Academy of Sciences, Datun Road 20A, Beijing 100101, People's Republic of China
[4] School of Science, Chongqing University of Posts and Telecommunications, Chongqing 400065, People's Republic of China
[5] Space sciences, Technologies and Astrophysics Research (STAR) Institute, Université de Liège, Allée du 6 Août 19C, 4000 Liège, Belgium

Received 2024 April 19; revised 2024 October 17; accepted 2024 October 18; published 2024 November 21

Abstract

KIC 6362386 is an eclipsing binary system that exhibits both γ Doradus (γ Dor)–type pulsations and starspots. In this study, we investigated this binary system using the Kepler photometry and the spectroscopic data from the Large Sky Area Multi-Object Fiber Spectroscopic Telescope. After employing the PHOEBE program for light-curve and radial-velocity-curve synthesis, analyses reveal that the binary is a circle ($e \sim 0.0006$), has a small mass ratio ($q \sim 0.311$), and is a detached system consisting of an F-type primary star and an M-type secondary star with masses and radii of $M_1 = 1.43 \pm 0.13\, M_\odot$, $R_1 = 1.68 \pm 0.08\, R_\odot$ and $M_2 = 0.44 \pm 0.18\, M_\odot$, $R_2 = 0.46 \pm 0.06\, R_\odot$, respectively. Utilizing the Padova isochrone, we estimate the age of the binary system to be $1.58^{+0.15}_{-0.13}$ Gyr. By analyzing the out-of-eclipse residuals, we identify variations in the residuals attributed to both starspots and stellar pulsations. The autocorrelation function analysis indicates the decay time of starspots is approximately 37 days with the rotation period aligning with the orbital period. Considering the masses, radii, and positions of the two components on the Hertzsprung–Russell diagram, we deduce that the γ Dor–type g-mode pulsations came from the primary star where the main frequency is 0.1642c/d. Consequently, KIC 6362386 becomes a valuable target for the investigation of γ Dor–type pulsations and asteroseismology in a binary system.

Unified Astronomy Thesaurus concepts: Starspots (1572); Stellar physics (1621); Gamma Doradus variable stars (2101); Pulsating variable stars (1307); Binary stars (154)

1. Introduction

Eclipsing binary stars are a special type of binary system where two stars orbit a common center of mass due to gravitational interaction, causing periodic mutual eclipses as seen from observers. This periodic brightness variation of binary stars allows scientists to accurately determine fundamental physical properties such as the masses, radii, and luminosities of the components and orbital parameters by analyzing their light curves and radial-velocity (RV) curves independent of models (G. Torres et al. 2010; N. A. Gorynya & A. Tokovinin 2014, X. Chen et al. 2024). For instance, eclipsing binaries provide an independent method for calibrating the extragalactic distance scale and thus determining the Hubble constant (A. Z. Bonanos 2006) and help determining the initial mass function (J. D. Kirkpatrick et al. 2024).

Many eclipsing binary stars have been discovered through successful survey projects such as Kepler (W. J. Borucki et al. 2010; A. Prša et al. 2011) and the Transiting Exoplanet Survey Satellite (TESS; G. R. Ricker et al. 2015). These surveys have generated massive data sets, providing high-precision time-series photometry. Additionally, the Large Area Multi-Object Spectroscopic Telescope (LAMOST) at the Xinglong Station of the National Astronomical Observatory in China has collected millions of spectral data (S.-G. Wang et al. 1996; X. Cui et al. 2010; X.-Q. Cui et al. 2012).

The LAMOST-Kepler (LK) project, initiated in 2012 to conduct follow-up spectroscopic observations for objects in the Kepler field, has acquired 766,425 low-resolution spectra (LRS) as of 2020 June (J. Fu et al. 2022). Furthermore, the LAMOST-Kepler medium-resolution survey (LK-MRS; W. Zong et al. 2020), launched in 2018, has significantly augmented these efforts. Consequently, integrating spectroscopic and photometric data offers a robust approach to studying the characteristics of eclipsing binaries within the Kepler field. This integration is pivotal for accurately determining their absolute stellar parameters, exploring stellar structures, and gaining new insights into evolutionary models (X. B. Zhang et al. 2017, 2018; K. G. Hełminiak et al. 2021).

In binary systems, starspot activity is an important area of study. Starspots are cooler regions on the stellar surface typically associated with strong magnetic fields (S. V. Berdyugina 2005). Photometric data allow researchers to determine the lifetime, amplitude, and longitudinal evolution of starspots. Variations in surface brightness due to rotational modulation caused by starspots provide insights into their decay timescale (H. A. C. Giles et al. 2017) and differential rotations (L. A. Balona & O. P. Abedigamba 2016; J. C. Lurie et al. 2017). The LK project has facilitated a series of studies on spotted detached eclipsing binaries. For instance, Y. Pan et al. (2020) investigated the short-period ($P \sim 4.4$ days) eclipsing binary KIC 8301013, identifying starspot modulation and revealing that the binary exhibits significantly stronger activity

Table 1
The Photometric Observation Information of KIC 6362386

Mission	Mode	Quarter/Sector	Start Time (BJD)	End Time (BJD)
Kepler	LC	Q0 ~ Q17	2454954.49956	2456423.49058
Kepler	SC	Q5	2455337.92332	2455371.17275
TESS	30 minutes	s14	2458683.53032	2458710.17659
TESS	10 minutes	s40, s41	2459390.74895	2459446.57554
TESS	10 minutes	s54, s55	2459769.90182	2459824.26260

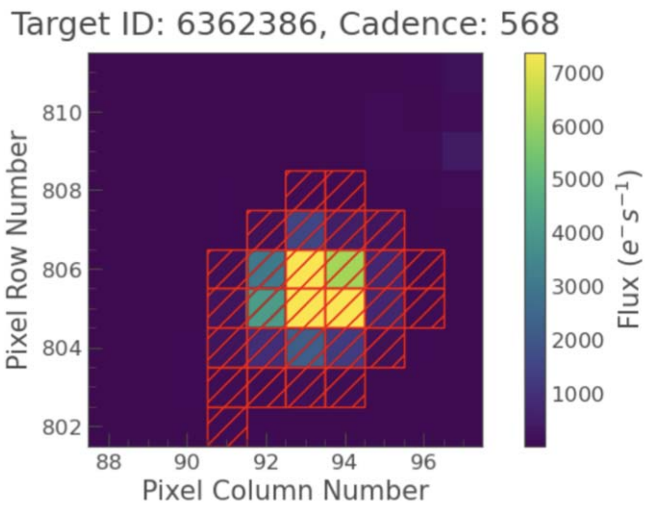

Figure 1. An example of the Kepler TPF file of KIC 6362386. The red squares stands for the aperture selected for photometry.

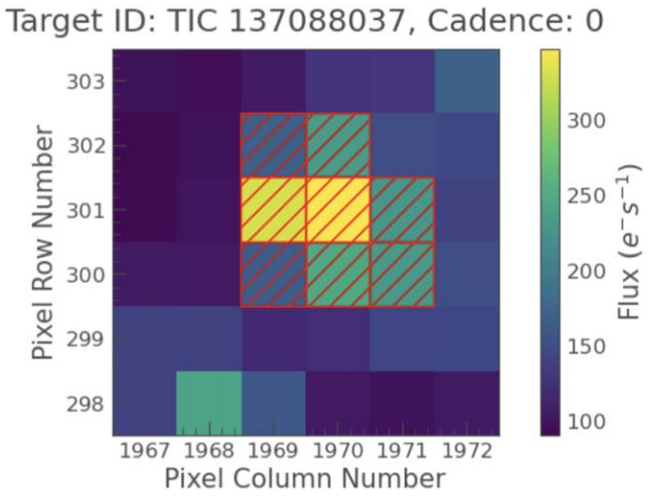

Figure 2. An example of the TESS FFI file of KIC 6362386. The red squares stands for the aperture selected for photometry.

levels compared to the Sun, aligning more closely with individual F-type stars. J. Wang et al. (2022) found that starspot sizes on 65% of binaries are smaller than the median size observed on single stars. The lifetimes of starspots on binaries are comparable to those on single stars when the rotation periods exceed 3 days.

γ Doradus (γ Dor) stars are main-sequence A- to F-type stars with typical masses ranging from 1.4 to 2.0 $M_{\odot}$ (A. B. Kaye et al. 1999; T. Van Reeth et al. 2016). These stars pulsate with gravity modes characterized by high radial orders ($20 < n < 100$) and low degrees ($l \leqslant 4$), with typical pulsation periods spanning from 0.3 to 3 days (L. A. Balona et al. 1994; H. Saio et al. 2018; G. Li et al. 2020).

Because these pulsations primarily probe the radiative region near the convective core boundary, γ Dor stars offer valuable insights into the deep stellar interior structure (S. A. Triana et al. 2015; T. Van Reeth et al. 2016). They provide a means to investigate the stellar interior. In recent years, the discovery of γ Dor stars in eclipsing binary systems has significantly increased (X. B. Zhang et al. 2018; X. Zhang et al. 2020). By leveraging precise parameters such as masses and radii derived from orbital motion and light eclipses of eclipsing binaries, detailed studies of γ Dor pulsations have been conducted for numerous systems under different contexts (M. A. Keen et al. 2015; Z. Guo et al. 2017; T. Van Reeth et al. 2023).

Our target is KIC 6362386, identified by Kepler with a period of approximately 4.6 days, was initially observed as a candidate with an exoplanet (W. J. Borucki et al. 2011). However, subsequent investigations utilizing various methods excluded the possibility of an exoplanet (J. L. Coughlin et al. 2014; T. D. Morton et al. 2016; D. J. Armstrong et al. 2017). In a later study, J. Zhang et al. (2019) sought to determine the parameters of mass, radius, and age of the primary star within the PARSEC isochrone (A. Bressan et al. 2012), employing the parameters derived from the LAMOST spectra. The resulting estimates were the mass of 1.37 $M_{\odot}$, the radius of 1.65 $R_{\odot}$, and the approximate age of 1.8 Gyr. D. Windemuth et al. (2019) utilized light-curve data, spectral energy distribution (SED), and stellar evolution models to derive binary parameters, without relying on RV curves. S. Sekaran et al. (2020) explored multiple binary systems, including KIC 6362386, and conducted preliminary research, unveiling the presence of a g-mode frequency at 0.1642c/d of KIC 6362386. Thus, KIC 6362386 is a valuable system that includes a pulsation component.

In this article, we conduct a detailed study on the binary system KIC 6362386, which has both pulsation and starspot activities. This article is organized as follows. In Section 2, information about the observations for the system is introduced. In Section 3, the physical parameters of the binary system are obtained. In Section 4, we analyze and discuss the residuals of the light curves of the binary system. Conclusions are provided in Section 5.

2. Data Collection

2.1. Photometric Data

The binary system KIC 6362386 underwent observations from both the Kepler and TESS missions. Kepler provided 18 quarters of long cadence (LC) data with a 30 minute exposure time, along with 1 quarter of the data of short cadence (SC) with a 1 minute exposure (A. Prša et al. 2011; B. Kirk et al. 2016). TESS, on the other hand, contributed one sector with a

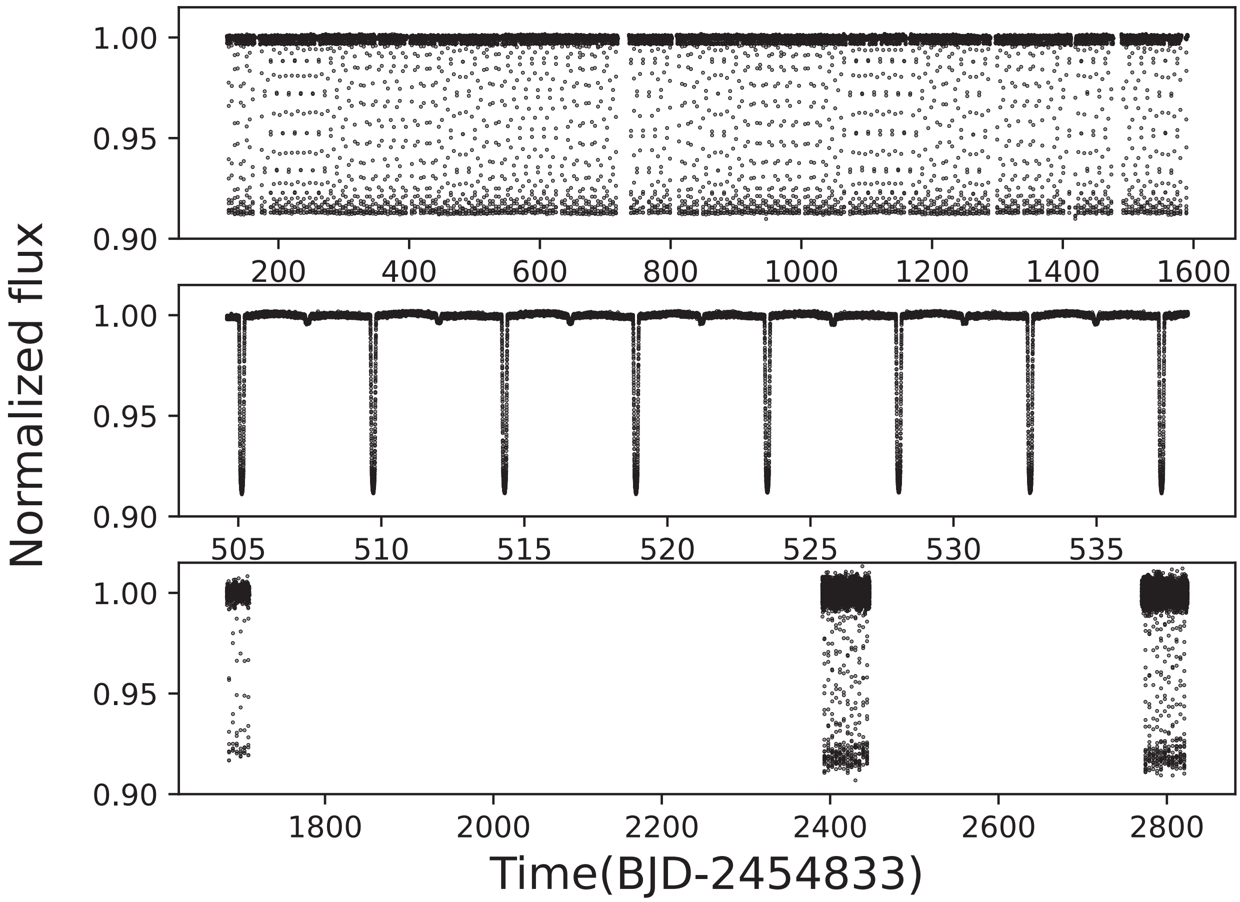

Figure 3. The light curve of KIC 6362386 observed by Kepler and TESS. The top, middle, and bottom panels show the light curves of data of all LC quarters, all SC quarters observed by Kepler, and all sectors observed by TESS, respectively.

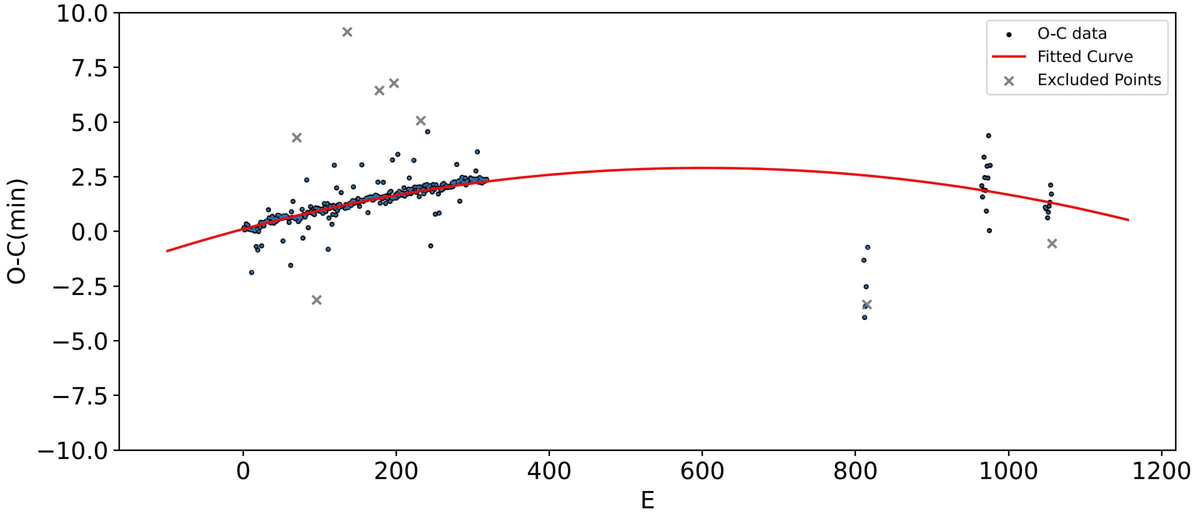

Figure 4. The $O-C$ diagram for KIC 6362386. The red line shows the fitting for the $O-C$ diagram. The outliers shown as the gray crosses are excluded in the fitting progress.

30 minute exposure time and four sectors with a 10 minute exposure time (G. R. Ricker et al. 2015). The detailed photometric data information can be found in Table 1.

Since the data quality obtained directly from the Mikulski Archive for Space Telescopes (MAST) website is relatively poor, the Lightkurve package in Python (Lightkurve Collaboration 2018) was employed to obtain the light curve by selecting the appropriate aperture from the Target Pixel File (TPF) provided by Kepler. Figure 1 shows the selected aperture for photometry. We extracted the light curve and performed normalization, detrending, and outlier removal. Prior to removing the outliers, we assessed their potential as flare signals, leveraging the similar processes from K. Xing et al. (2024). The analysis did not reveal any flare signals in this binary system. Since TESS data are not always provided with predetermined apertures in TPF but rather as full-frame images

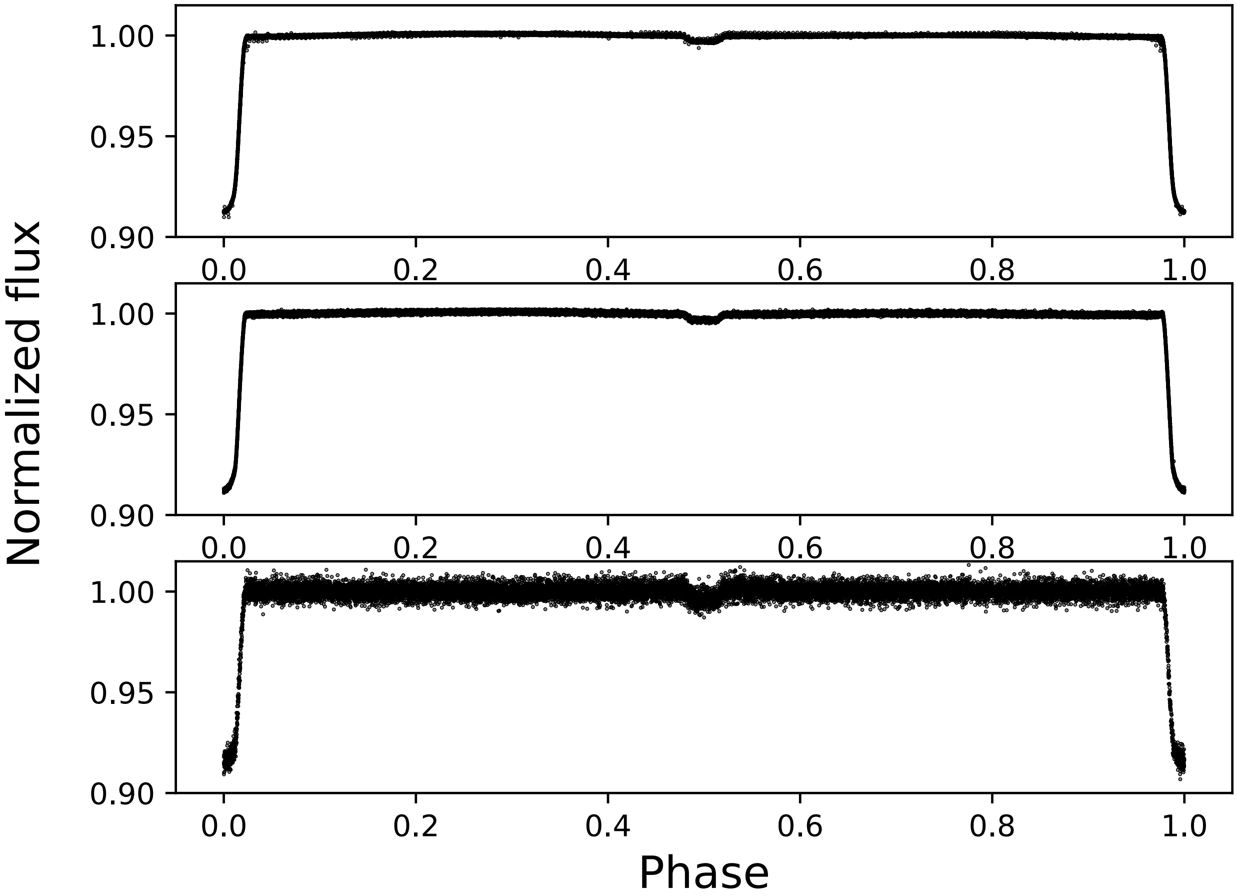

Figure 5. The phase-folded light curves of KIC 6362386 from the photometry. The top, middle, and bottom panels stands for the data from Kepler LC quarters, SC quarters, and TESS sectors, respectively.

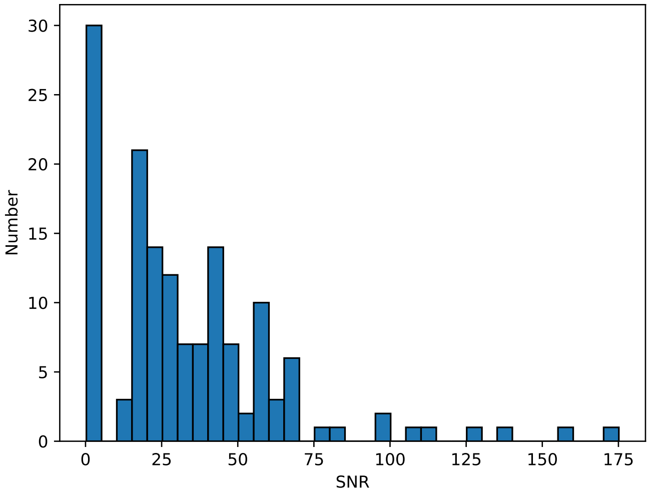

Figure 6. The distribution of SNR of a total of 146 spectra.

(FFIs), users must determine the aperture themselves. In our study, we utilized the "cutout" command from the lightkurve package to extract the region of interest from the FFI images of TESS data, and selected the pixels marked by the red squares as the aperture for light-curve extraction as shown in Figure 2. The final light curve is shown in Figure 3.

The period was calculated based on the obtained light curve, which is 4.5924 ± 0.0007 days, and BJD0 (2454837.55341 ± 0.00069 days) was subsequently determined using this period. The final $O - C$ diagram is shown in Figure 4. The quadratic fitting shows

$$O - C(\text{min}) = (-7.73 \pm 0.01) \times 10^{-6} \cdot E^2 + (9.31 \pm 0.04) \times 10^{-5} \cdot E + (0.101 \pm 0.005). \quad (1)$$

The quadratic term in Equation (1) reveals a continuous period decrease (the red solid line in Figure 4) at a rate of

$$\frac{dP}{dt} = (-7.59 \pm 0.03) \times 10^{-14}\ \text{day yr}^{-1}.$$

Using this information, we generated the phase-folding light curves of the binary system, as shown in Figure 5. The phase-folded light curves enable a clear morphological classification of KIC 6362386 as a detached binary system, indicating that neither star fills its Roche lobe.

2.2. Spectroscopic Observations

KIC 6362386 is a target of the LAMOST-Kepler project (P. De Cat et al. 2015), leading to the acquisition of low-resolution spectra (LRS; resolution ∼1800) and medium-resolution spectra (MRS; resolution ∼7500) in the LAMOST database. Within the LRS data set, two spectra with signal-to-noise ratios (SNRs) exceeding 200 provide reliable stellar atmosphere parameters. The uncertainties for parameters are obtained from J. Wang et al. (2020). The MRS data set, comprising a total of 146 spectra, exhibited a subset of 116 spectra with an SNR greater than 10 based on the analysis in

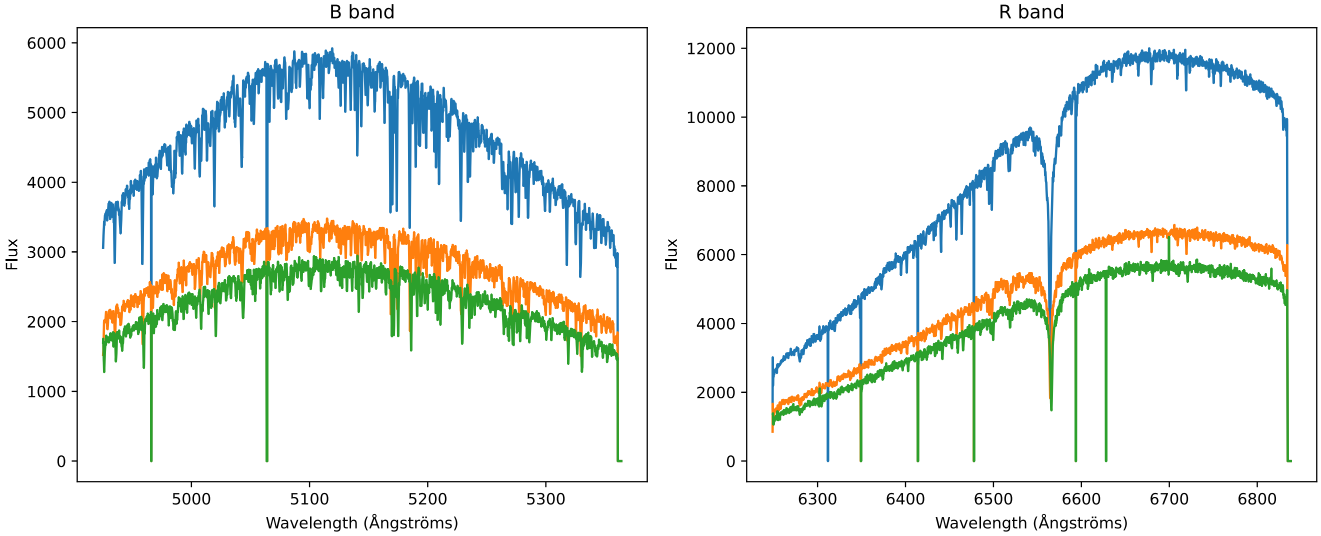

Figure 7. Three examples of MRS for KIC 6362386.

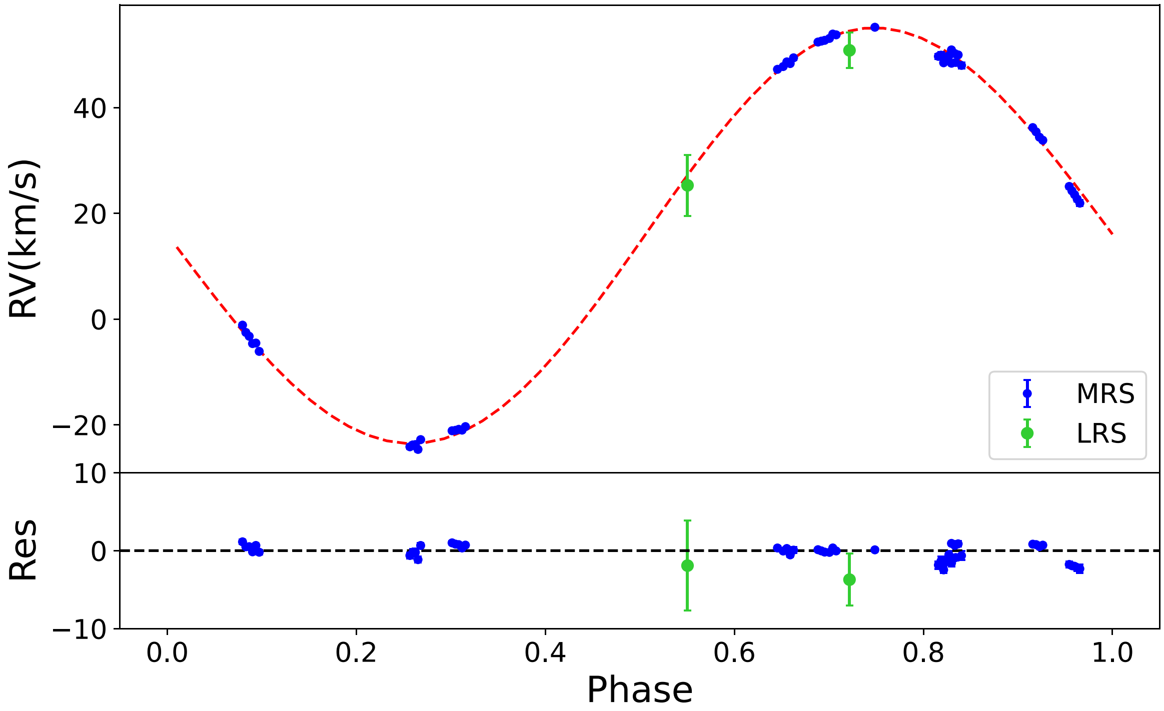

Figure 8. The RV curve of KIC 6362386. The red dashed line represents the best-fit curve resulting from the fitting process.

Table 2
The Spectroscopic Data of KIC 6362386

Mode	Wavelength Coverage	Visits	Average SNR	$T_{\rm eff}$ (K)	(Fe/H)	logg
LRS	370 ∼ 900 nm	2	207.05	7000 ± 112	−0.16 ± 0.14	4.12 ± 0.08
MRS	495 ∼ 535 nm(B) & 630 ∼ 680 nm(*R*)	146	42.54	/	/	/

Note. The uncertainties of parameters are obtained from J. Wang et al. (2020).

W. Zong et al. (2020). The distribution of the SNR is shown in Figure 6, and a sample of the spectra is shown in Figure 7. Detailed information about the spectroscopic observation is provided in Table 2. Based on the methodology outlined by B. Zhang et al. (2021), the RVs of KIC 6362386 were extracted. Specifically, B. Zhang et al. (2021) employed the cross-correlation function (CCF; J. Tonry & M. Davis 1979) to identify the optimal template match and adopted the corresponding RV as the initial estimate for the final RV determination. To obtain the final RV, they maximized the CCF using the

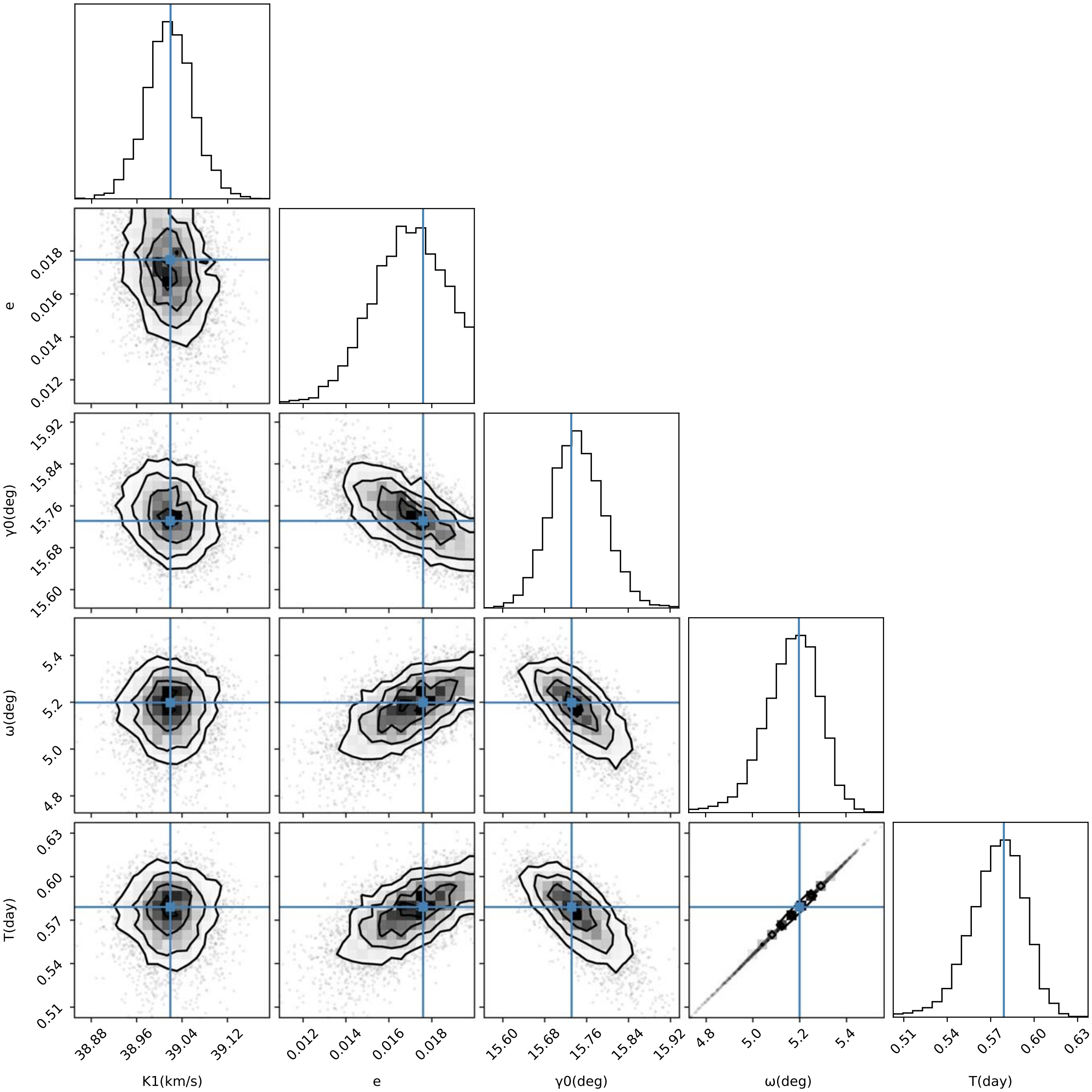

Figure 9. The corner diagram of the RV curve fitting.

scipy.optimize.minimize optimization routine, incorporating the NelderMead algorithm (J. A. Nelder & R. Mead 1965). Measurement errors were estimated using the Monte Carlo method, which involved repeating the entire process 100 times, with each iteration introducing Gaussian random noise based on the flux error. This approach ensured a robust and reliable determination of the RVs for KIC 6362386. The RV curve is depicted in Figure 8. The substantial difference in the depths of eclipses (approximately 0.09) between the primary and secondary components of KIC 6362386 (see Figure 5), which means there exists a considerable effective temperature difference between the primary and secondary stars, results in only the primary star being observable in the spectra, leading to a single RV curve. The blue data points represent RV obtained from MRS, while the green data points denote RV provided by LRS; the correction function of the RV value of LRS is obtained from J. Wang et al. (2020), which compared the RV of LRS with APOGEE and Gaia for the same targets. The function is shown as follows:

$$\mathrm{RV}_{\mathrm{cor}} = (1.00 \pm 0.01) \times \mathrm{RV}_{\mathrm{LRS}} + (5.01 \pm 1.05)\mathrm{km\ s}^{-1}. \tag{2}$$

The RV data of LRS effectively fill the gap in the phase around 0.5. Equations from R. W. Hilditch (2001) shown as follows were employed to fit the RV curve and yielding the parameters:

Kepler's equation:

$$E - e\sin E = 2\pi(t - T)/P; \tag{3}$$

Table 3
Orbital Solution and Physical Parameters of KIC 6362386

Parameter	Primary	System	Secondary
BJD0(day)		2454837.55341 ± 0.00069	
$P_{\rm orb}$ (day)		4.5924 ± 0.0007	
e		0.00063 ± 0.00034	
K (km $\rm s^{-1}$)		39.31 ± 0.04	
γ_0 (km $\rm s^{-1}$)		15.54 ± 0.05	
ω (deg)		5.02 ± 0.18	
q (M2/M1)		0.31 ± 0.07	
i (deg)		87.71 ± 0.37	
a ($R_\odot$)		14.32 ± 0.08	
Mass ($M_\odot$)	1.43 ± 0.13		0.44 ± 0.18
Radius ($R_\odot$)	1.68 ± 0.08		0.46 ± 0.06
$T_{\rm eff}$ (K)	7000 ± 150		3490 ± 120
logg (cgs)	4.15 ± 0.14		4.78 ± 0.05
Gravity-darkening exponent	0.32		0.32
Limb-darkening coefficient	[0.29,0.42]		0.5

relationship between the true and eccentric anomalies:

$$\tan(\theta/2) = [(1+e)/(1-e)]^{1/2}\tan(E/2); \tag{4}$$

the final expression for RV:

$$V_{\rm rad} = K_1[\cos(\theta+\omega) + e\cos\omega] + \gamma_0, \tag{5}$$

where E is the eccentric anomal, T is the time of periastron passage, P is the orbital period, K_1 is the semiamplitude of the RV curve, γ_0 is the systemic velocity, ω is the pericentric angle, and e is the eccentricity. We need to solve for five parameters: K_1, T, γ_0, ω, and e. From the spectra, we obtain the RV $V_{\rm rad}$ and the corresponding phase t. These values serve as known conditions, with Equation (4) acting as the fitting curve equation. We utilized the Python package `emcee` to perform the Markov Chain Monte Carlo (MCMC) simulation. The MCMC was run with 5000 steps, 6 parallel chains, and 2000 burn-in steps. The corner plot showing the posterior distributions of the parameters is displayed in Figure 9. These parameters are detailed in Table 3.

3. Binary Modeling and Parameter Determination

Combining both the photometric and the spectroscopic data, we employed the PHysics Of Eclipsing BinariEs (PHOEBE) program for modeling (A. Prša & T. Zwitter 2005; A. Prša et al. 2016; D. Jones et al. 2020). The initial ranges for various parameters were set, with fixed values for the orbital period of $P_{\rm orb} = 4.5924$ days and $\rm BJD_0 = 2454837.55341$ days. The parameters such as the masses and the radii of both stars (M_1, M_2, R_1, R_2), the temperature of stars (T_1, T_2), and the eccentricity (e) were kept as free parameters.

To optimize the modeling accuracy, particularly in the eclipse section with a high sampling rate, we employed Kepler SC data. Prior to inputting the light-curve data, we utilized Gaussian processes to eliminate signals that may be caused by starspots or pulsations, ensuring a clean light curve for precise parameter determination (C. E. Rasmussen & C. K. I. Williams 2006). This method assumes that the joint probability distribution of the observational data is a multivariate Gaussian distribution with a covariance matrix described by a covariance function, known as the Gaussian Process (GP) kernel. Finding an appropriate GP kernel is a crucial step in this process. We use a GP kernel adopted by R. Angus et al. (2018) to model starspots and infer stellar rotation periods. The GP kernel is described as follows:

$$k_{i,j} = A\exp\left[-\frac{(t_i-t_j)}{2l^2} - \Gamma^2\sin^2\left(\frac{\pi(t_i-t_j)}{P}\right)\right] + \sigma^2\delta_{ij}, \tag{6}$$

where $k_{i,j}$ is the covariance between the ith and the jth data. t_i and t_j are the epochs of the ith and the jth data, respectively. Here A, l, Γ, P, and σ are free parameters. The optimal parameters are derived using the Python module *SCIKIT − LEARN*[3] (F. Pedregosa et al. 2011). The model is then extrapolated to the entire phase after the optimal parameters are determined. Finally, these modeled signals are subtracted from the light curves. The MCMC was adopted during the modeling process to refine iteratively the range of the free parameters; we first used the emcee package for MCMC analysis with 5000 steps, 10 parallel chains, and 3000 burn-in steps. In this step, our goal was to obtain a reasonable parameter range to lay the groundwork for subsequent steps. Therefore, we only needed to achieve a relatively convergent result. Achieving full parameter convergence would take an extremely long time due to the model's complexity. The corner plot is shown in Figure 10. After obtaining the parameter range, we used PHOEBE's built-in Levenberg–Marquardt algorithm to determine the final parameters.

The quadratic limb-darkening (QLD; A. Claret & S. Bloemen 2011) model assumes that the brightness ($I(\mu)$) at a given angle (μ) (which is usually defined as ($\cos\theta$), where (θ) is the angle between the line of sight and the normal to the stellar surface) can be approximated by a quadratic polynomial:

$$I(\mu) = I_0(1 - a(1-\mu) - b(1-\mu)^2). \tag{7}$$

Here, (I_0) is the brightness at the center of the star (($\mu = 1$)), and (a) and (b) are the QLD coefficients. Gravity darkening is a phenomenon that occurs in rapidly rotating stars where the star is not a perfect sphere due to centrifugal forces. This leads to a variation in surface gravity from the poles to the equator. The poles experience higher gravity and are hotter and brighter, while the equator, with lower gravity, is cooler and dimmer. The gravity-darkening coefficient (usually denoted as β) quantifies this effect. In mathematical terms, the brightness I at a point on the star's surface depends on the local effective gravity g as follows (A. Claret & S. Bloemen 2011):

$$I \propto g^\beta. \tag{8}$$

An initial difference was observed between the observed and the theoretical light curves during the primary eclipse phase. Considering that the secondary star is in front of the primary star during this phase, the total surface brightness variation is influenced by the distribution of surface brightness of the primary star. To account for this, we kept the limb-darkening coefficient of the primary star as a free parameter in the binary system. Multiple iterations of fitting led to the optimal solution.

This optimal solution was served as the initial solution for modeling the Kepler LC and TESS data for each quarter/sector. We performed the fitting for each quarter/sector to

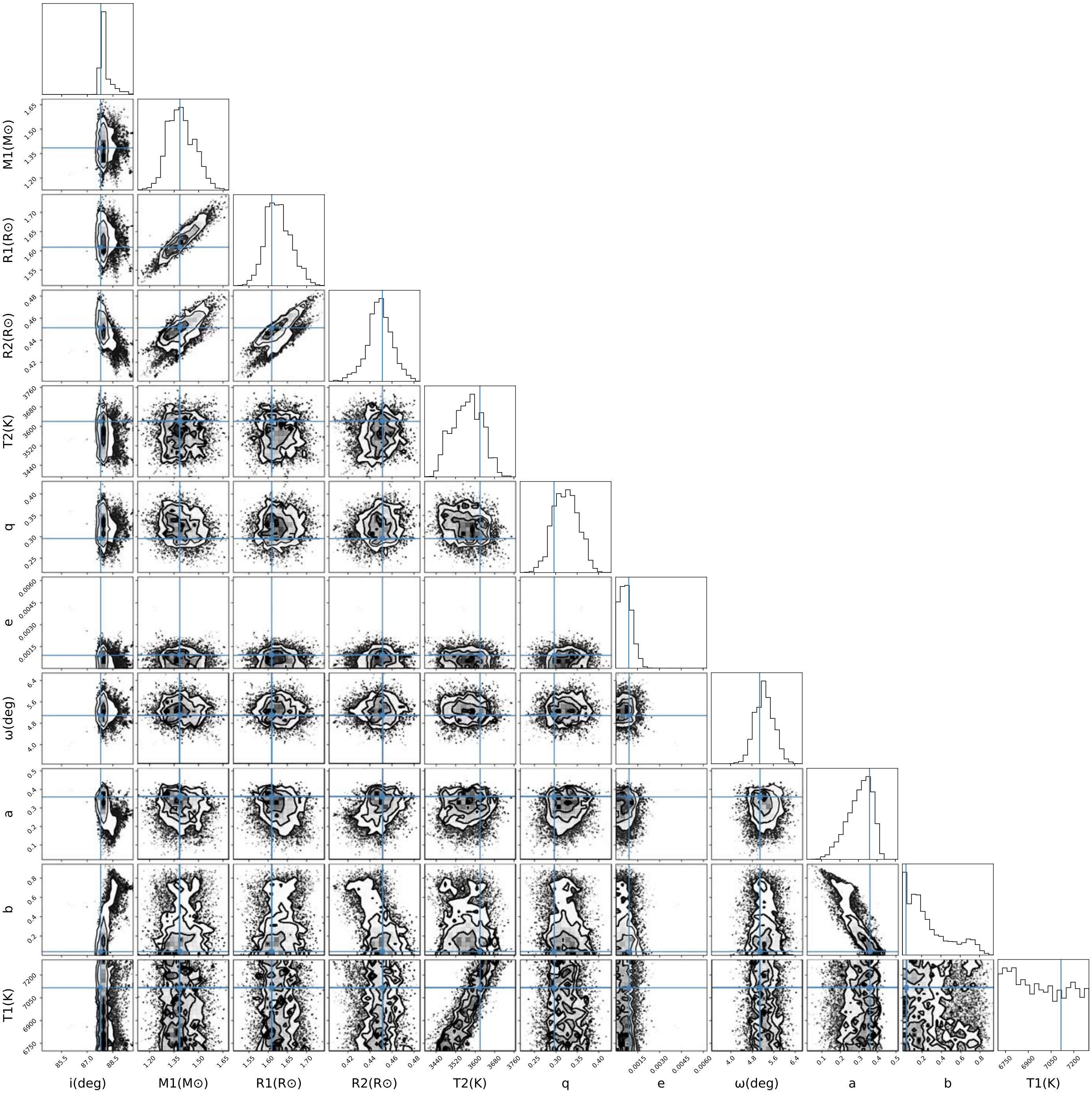

Figure 10. The corner diagram of the MCMC results.

obtain the parameters. In PHOEBE, it is possible to set the exposure time and wavelength band for fitting, which can be configured in the PHOEBE fitting program. Different exposure times and wavelength bands can be set according to the parameters to be fitted. Aggregating all optimal solutions, we derived the orbital and physical parameters of the binary system, as listed in Table 3. The fitted light curves as well as the residuals are shown in Figure 11.

By combining the physical parameters obtained from the binary system modeling with the atmospheric parameters from the LAMOST spectra, we determined the system's age using the Padova isochrone (A. Bressan et al. 2012). The result is depicted in Figure 12. The solid line denotes the measured metal abundance of the isochronous line (-0.16 dex), while the dashed line represents the isochronous line with a metal abundance of -0.16 ± 0.14 dex. The logarithm of the age ($\log t$) of KIC 6362386 was determined to be $9.20^{+0.04}_{-0.04}$ dex. According to the evolutionary stage mark of the Padova isochrone, the primary star is a main-sequence star, while the secondary star is a pre-main-sequence star, with a slightly slower evolution than the primary star.

The data from Gaia (Gaia Collaboration et al. 2023) revealed a parallax of 0.981 ± 0.012 mas for KIC 6362386. Utilizing the distance and luminosity calculation method by

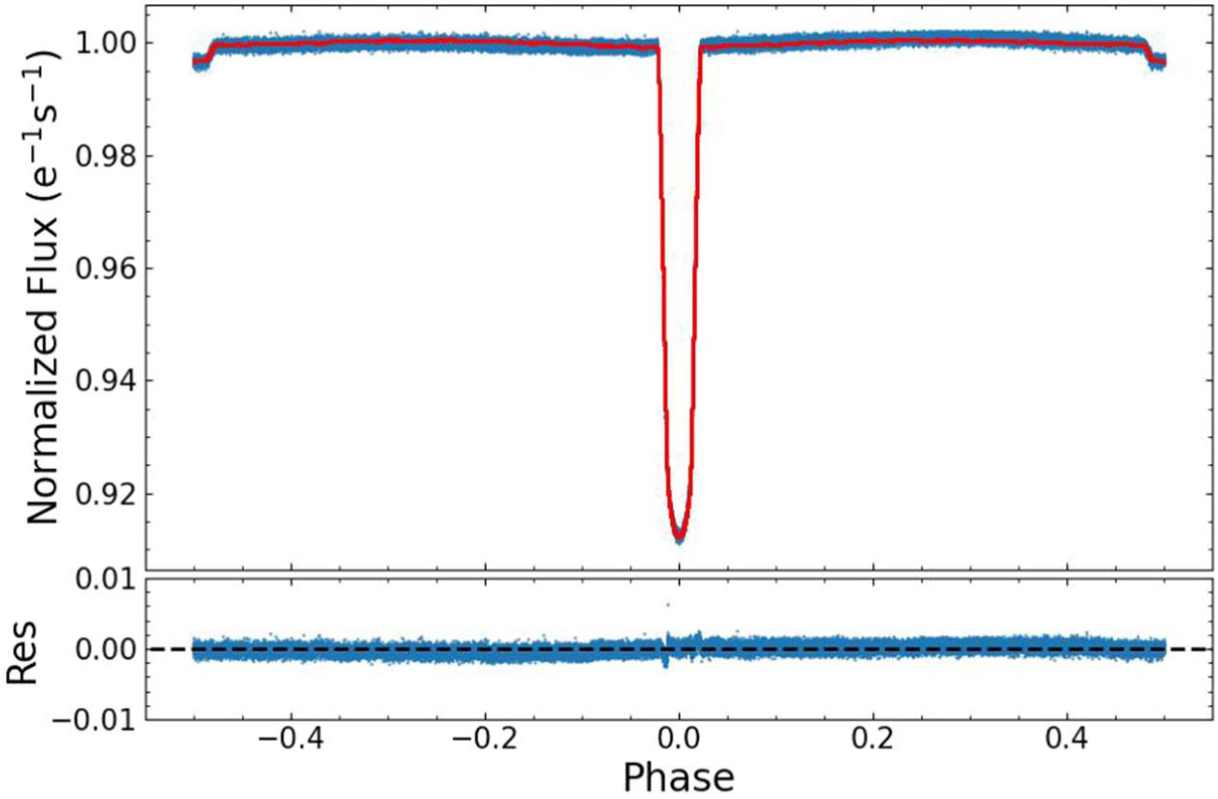

Figure 11. The light curves of KIC 6362386 from the Kepler SC photometry fitted under the optimal solution in the upper panel. The residuals are shown in the lower panel.

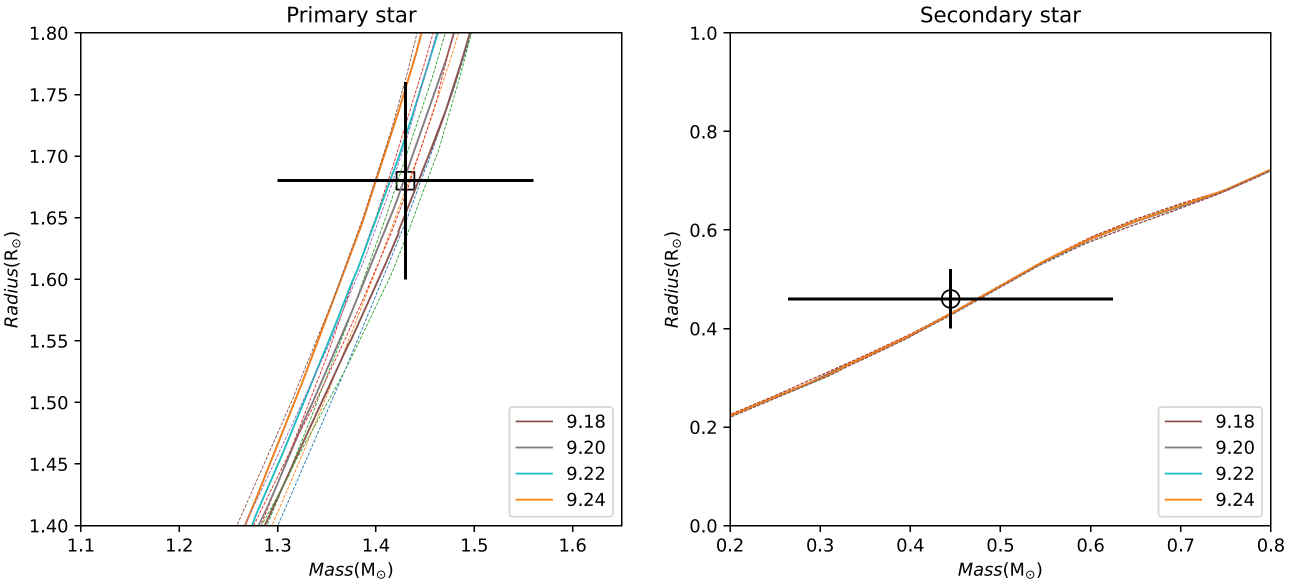

Figure 12. The fitting isochrones of KIC 6362386. The square and circle denote the locations of the primary and secondary, respectively. The solid lines show the isochrones with metallicity of [Fe/H], which is −0.16 dex derived from the spectra. The color of the line represents the logarithm of the age of the binary system $\log t$. The dashed lines show the isochrones with metallicity of [Fe/H]$\pm\, \sigma_{[\mathrm{Fe/H}]}$, which are -0.16 ± 0.14 dex.

C. A. L. Bailer-Jones et al. (2018), we determined a distance of 1019 ± 12 pc and an absolute luminosity of $6.87 \pm 0.21\, L_\odot$ for KIC 6362386. The equation we use to calculate the absolute luminosity is from C. A. L. Bailer-Jones et al. (2018):

$$M = M_G + 5(1 - \log d) - A_G \tag{9}$$

$$-2.5 logL = M + BC_G(T_{\mathrm{eff}}) - M_{\mathrm{bol},\odot}, \tag{10}$$

where M and $MG = 12.82$ mag are the absolute magnitude and apparent magnitude in the G band of Gaia, respectively. The extinction coefficient AG in Equation (6) is 0.2124 in the G band (C. A. L. Bailer-Jones et al. 2021). The parameter $M_{\mathrm{bol},\odot}$ is the bolometric magnitude of the Sun, which is defined by the IAU and its value is 4.74 mag (E. E. Mamajek et al. 2015). $BC_G(T_{\mathrm{eff}})$ is the bolometric correction, which depends only on

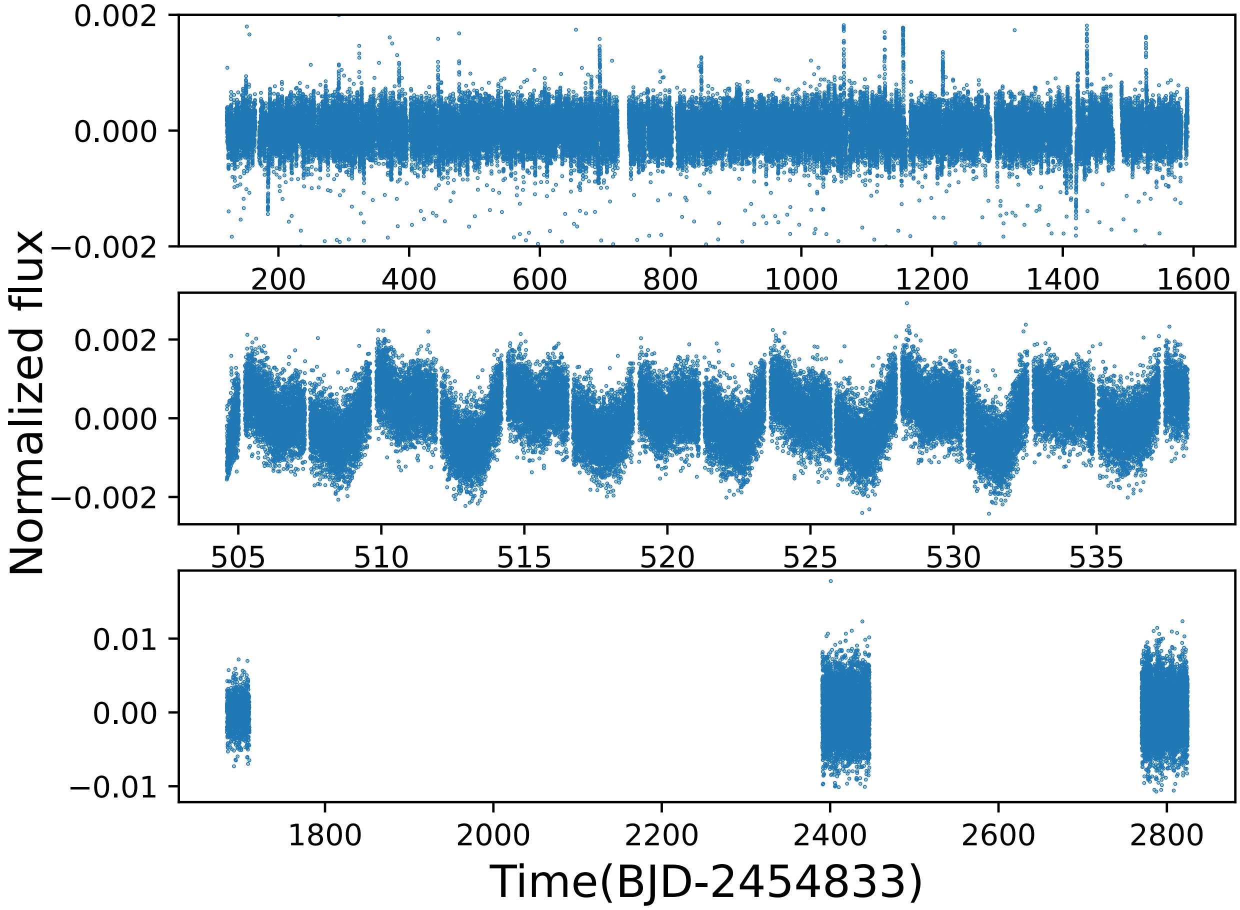

Figure 13. The out-of-eclipse residuals of KIC 6362386. The top, middle, and bottom panels show the residuals from the Kepler LC photometry, the Kepler SC photometry, and the TESS photometry, respectively.

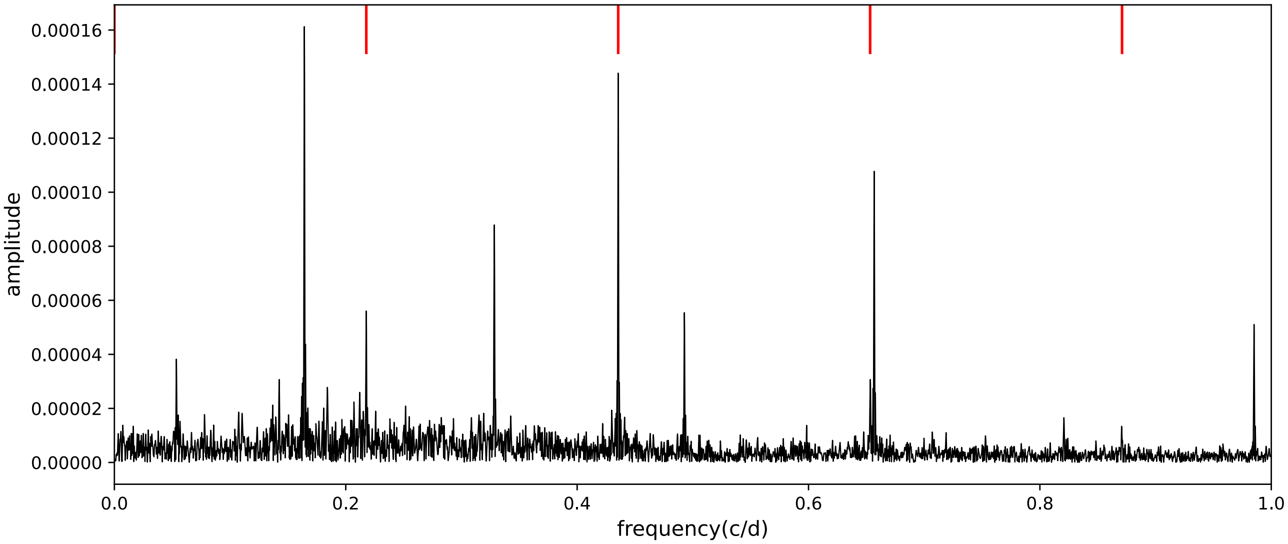

Figure 14. The fast Fourier transform (FFT) of the removed binary orbital frequency of KIC 6362386 LC data. The red lines indicate the frequencies of the orbital frequency of KIC 6362386 and its harmonic frequencies.

the effective temperature (R. Andrae et al. 2018). The cumulative parameters of the binary from our orbit analysis amounted to $6.11 \pm 0.70\ L_{\odot}$, aligning well with the binary luminosity obtained from Gaia.

4. Residual Analysis

Using the parameters derived from the PHOEBE orbit analysis, we examined the residuals between the observed and modeled light curves of KIC 6362386. To ensure the accuracy

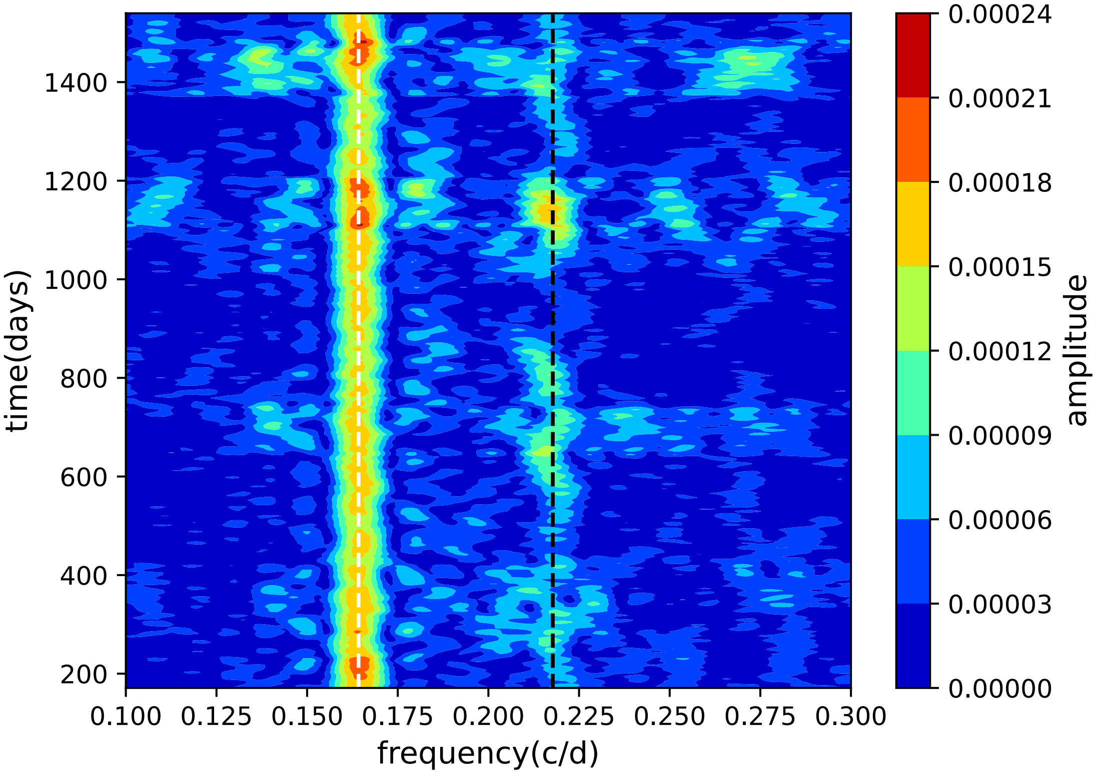

Figure 15. The sFT of KIC 6362386 LC data with the white dashed line representing the frequency of 0.1642c/d and the black dashed line indicating the binary orbital frequency.

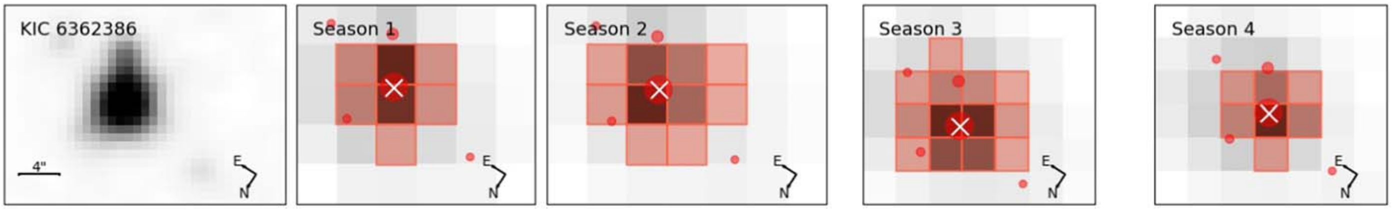

Figure 16. The surrounding stars of KIC 6362386 made by `tpfi` (K. Xing et al. 2024). The image on the far left is the binary identification chart, while the others are the TPF files for each season. The red region indicates the default aperture mask, with the target denoted by a white cross symbol.

of the residual signal analysis, we focused on the out-of-eclipse residuals for a detailed investigation, as shown in Figure 13.

Conducting Fourier analysis on the out-of-eclipse residuals allowed us to identify signals present in the data, as shown in Figure 14. The red lines indicate the orbital frequency and the harmonic frequencies of the binary. Interestingly, additional frequencies were observed alongside the orbital frequency. To assess the stability of the signals, we introduced the sliding Fourier transform (sFT) for evaluation (W. Zong et al. 2016a, 2016b). We configured the sliding step to be 10 days and the window size to be 100 days. Due to the limited duration of the Kepler SC and TESS data, the sFT analysis holds less significance for these data sets. Therefore, we exclusively conducted this operation on the Kepler LC data, as showcased in Figure 15. From the graph, we can observe a frequency-stable yet amplitude-varying signal near the white dashed line, while the signal near the black dashed line shows some instability.

To account for the presence of these frequencies, we considered three potential factors: surrounding star pollution, starspot activity, and pulsations.

4.1. Surrounding Star Pollution

Our initial consideration focused on the possibility that the observed signals originated from the contamination by surrounding stars. The TPF images show the presence of two neighboring stars in proximity to our target binary system, KIC 6362386, as illustrated in Figure 16. If these neighboring stars exhibit pulsations, it could influence the brightness of KIC 6362386. To investigate this, we carefully selected the aperture to extract and analyze the light curves of these two neighboring stars. The results, displayed in Figure 17, revealed no prominent frequencies after whitened orbital frequency and its harmonics. We found the relevant information about the surrounding stars in Gaia listed in Table 4. The magnitude of KIC 6362386 is around 12 mag, and the effective temperature is around 7000 K. Based on the magnitude, the surrounding stars brightness is over 100 times less than the target star. And the effective temperature of the surrounding stars are around 4800 K, which is much lower than KIC 6362386. Thus, the probability of surrounding stars affecting the target star is extremely low, and the lights for the surrounding stars could mostly be from the light of

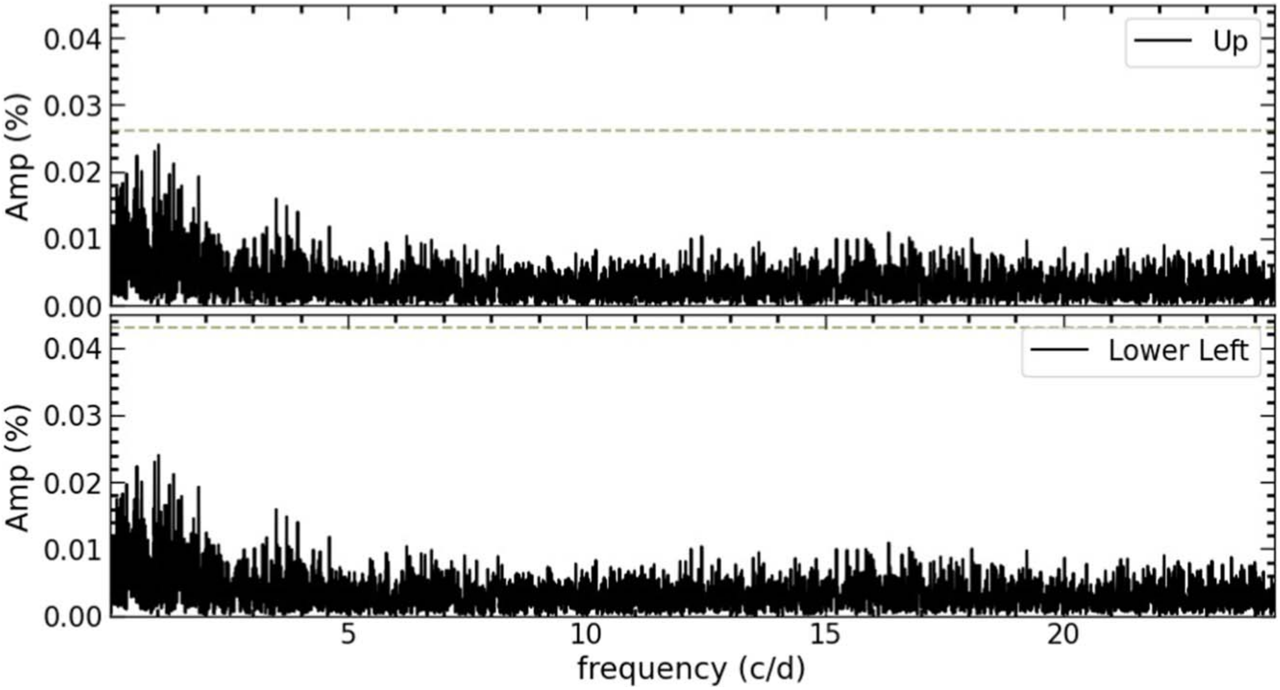

Figure 17. FFT of whitened orbital frequency and its harmonics. The horizontal axis represents frequency (c/d), the vertical axis represents amplitude (amplitude in % of the mean brightness vs. frequency in μHz), and the dashed horizontal line refers to the 5σ detection threshold of local noise level. The upper panel is the FFT of the star located above the target star, while the lower panel is the FFT of the star located to the lower left of the target star.

Table 4
Information about the Surrounding Stars from Gaia

source_id	R.A.	Decl.	phot_g_mean_mag	bp_rp	teff_gspphot (K)
2101722626891070000	291.2673606	41.74827732	18.913	1.072	4880
2101722626891720000	291.2649821	41.7502741	18.594	2.2901	
2101722626891720000	291.2652427	41.74760892	17.179	1.123	4750
2101722631184770000	291.2624672	41.74731476	20.217	1.733	

KIC 6362386. Consequently, we can confidently conclude that the observed periodic variations in KIC 6362386 are not due to the neighboring stars.

4.2. Starspot

Notably, the brightness of the two out-of-eclipse segments in KIC 6362386 exhibits a discernible disparity as shown in Figure 18, indicative of a clear O'Connell effect (D. J. K. O'Connell 1951). The evident asymmetry in the light curve is often linked to stellar spots, hot spots resulting from mass transfer between two components, or circumstellar matter. In the case of KIC 6362386 being a detached binary system with no material exchange, we ruled out the possibility of hot spots. Simultaneously, direct evidence of material around the star, such as spectral characteristics of cold dust, has not been observed in the LAMOST spectrum. Consequently, the light-curve asymmetry of KIC 6362386 is highly likely attributed to starspots. Based on the sFT of the out-of-eclipse residual light curve as shown in Figure 15, we can see the frequencies changes around 0.2177c/d, which we believe are caused by starspot activity.

To derive relevant parameters of the starspot activity, we employed an autocorrelation function (ACF) analysis (A. McQuillan et al. 2014; H. A. C. Giles et al. 2017). The ACF behavior exhibits characteristics similar to underdamped harmonic oscillators (uSHO) in a relatively short time lag stage (H. A. C. Giles et al. 2017). Thus, the core equation for the autocorrelation function is expressed as follows:

$$y(t) = \mathrm{e}^{(-t/\tau_{\mathrm{AR}})}\left[A\cos\left(\frac{2\pi t}{P}\right) + B\cos\left(\frac{4\pi t}{P}\right) + y_0\right]. \quad (11)$$

Here, τ_{AR}, P, A, B, and y_0 represent the decay timescale of ACF, the stellar rotation period, the amplitudes of the two cosine terms, and the offset, respectively (H. A. C. Giles et al. 2017).

In order to find the optimal fitting for the starspot parameters, the EMCEE code (D. Foreman-Mackey et al. 2013) was employed to fit the ACF of the residuals to derive the parameter values. The fitting results revealed that the decay timescale of the starspots was approximately 37 days, while the rotation period was around 4.5973 days, closely aligning with the orbital period $P_{\mathrm{orb}} = 4.5924$ days of the binary star. An illustrative example of the fitting result is depicted in Figure 19.

Based on the parameters of KIC 6362386, we calculated the synchronization timescale for the binary system according to R. W. Hilditch (2001). The formulae are shown as follows:

$$t_{\mathrm{sync}} \approx 10^4\left[\frac{1+q}{2q}\right]^2 P^4 \mathrm{years}, \quad (12)$$

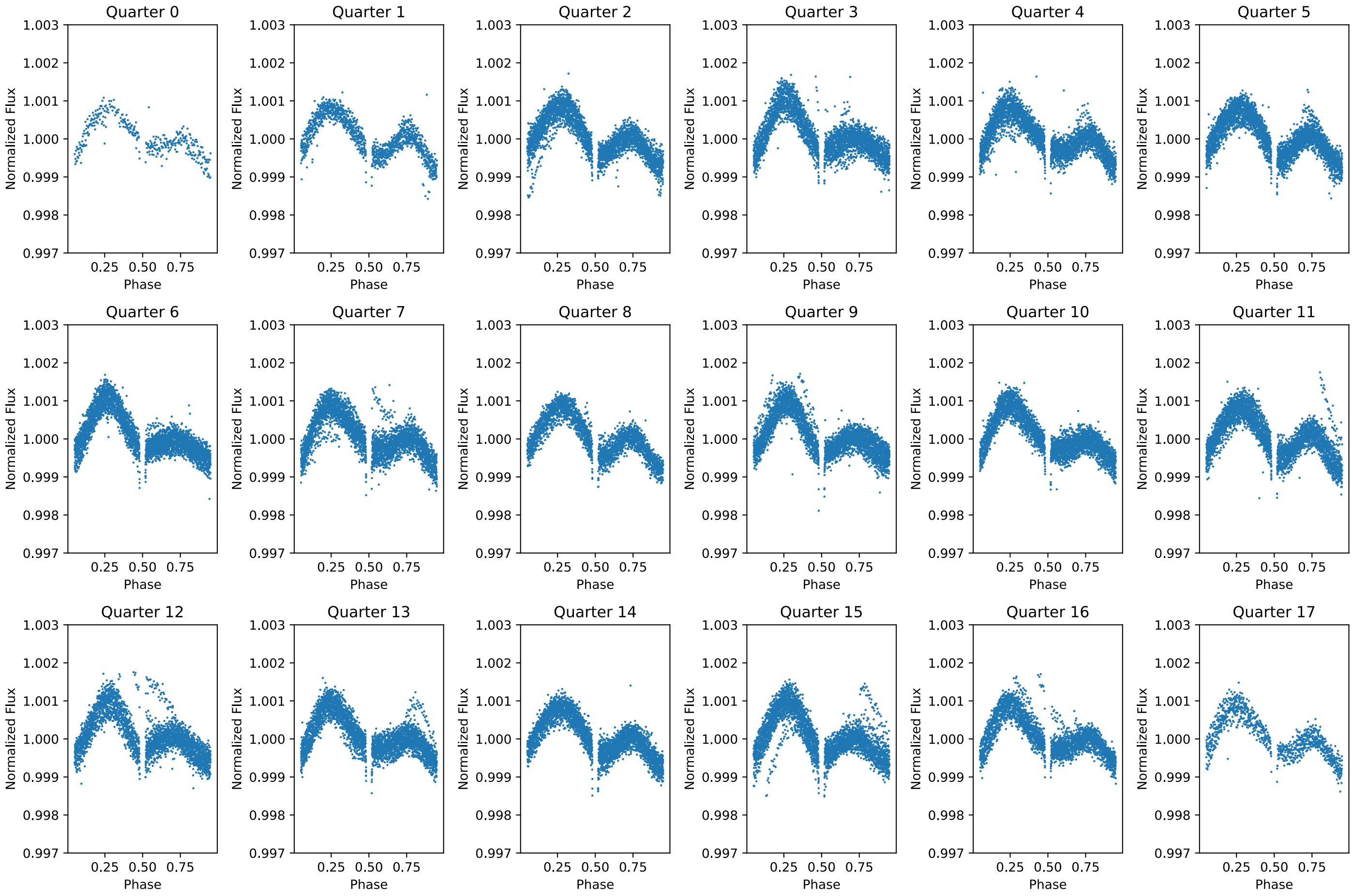

Figure 18. The diagram of out-of-eclipse light curves. Each subplot corresponds to one quarter in Kepler LC data.

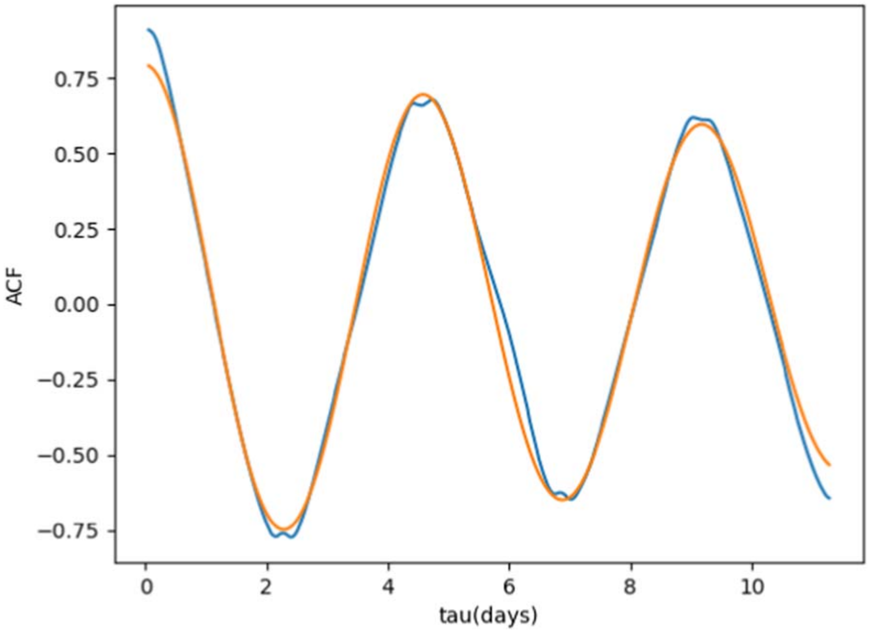

Figure 19. The ACF of the residuals of the light curves of KIC 6362386. The blue curve represents the ACF, and the orange curve represents the best-fitting result obtained through the corresponding MCMC analysis. The consistency between the results of ACF and MCMC proves the presence of spots with a rotational period consistent with the orbital period of KIC 6362386.

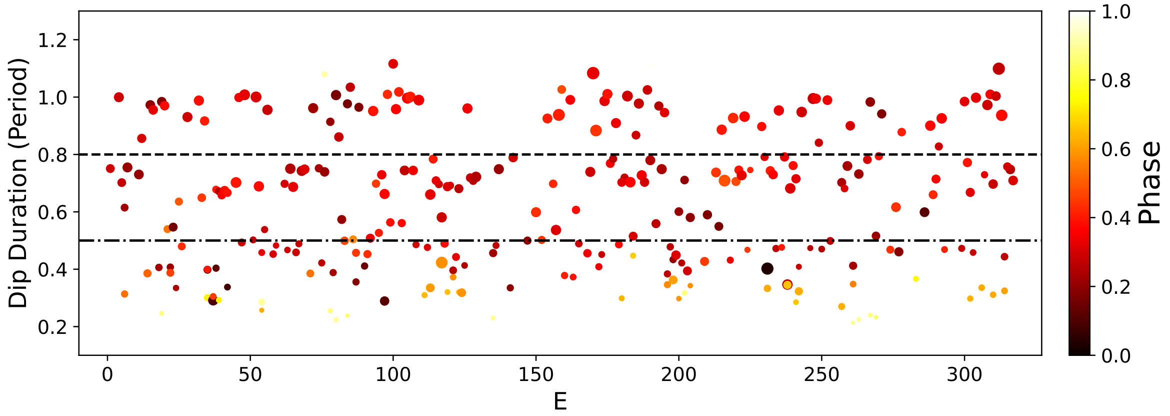

Figure 20. The SDR of the residuals of KIC 6362386. In this figure, each dot's size represents the depth of the starspot, while the color signifies the phase where each starspot dip occurs. The dotted–dashed line delineates the dip duration of half a period, and the boundary between a single starspot and a double starspot is represented by a dashed line.

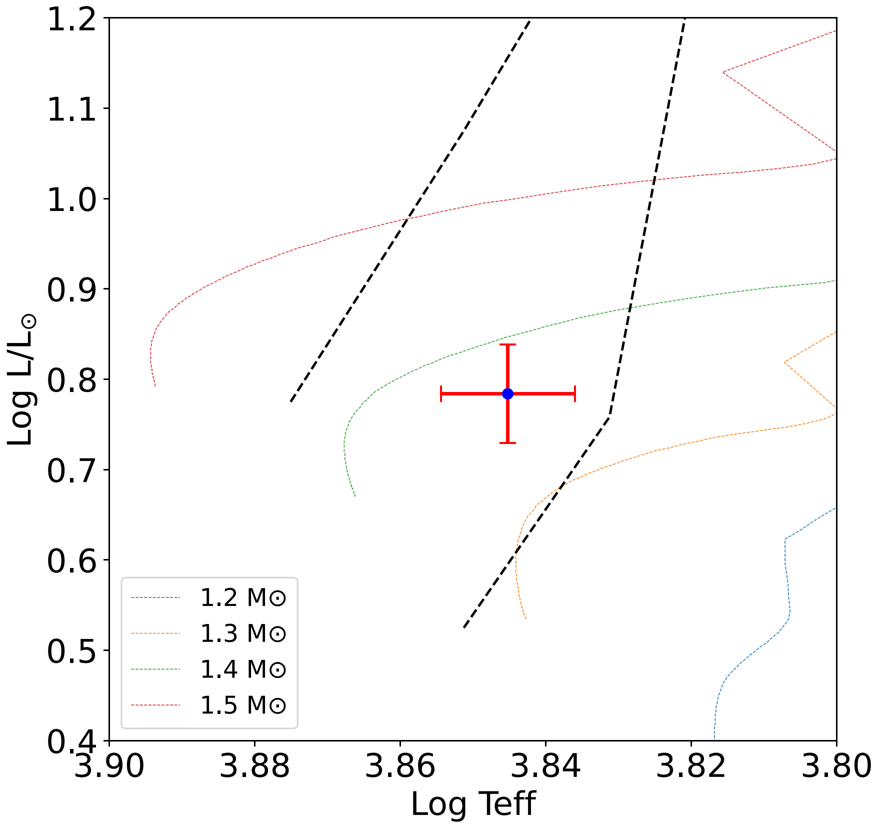

Figure 21. The H-R diagram of the primary star of KIC 6362386. The blue point indicates the location of the primary star. The black dashed lines show the theoretical instability strip of γ Dor stars (G. Li et al. 2020; M. A. Dupret et al. 2005). The solid lines in the figure represent the evolutionary tracks of stars with different masses.

where P is the orbital period in days and q is the mass ratio. Thus, we obtained a synchronization timescale around 0.20 Gyr. The age of the binary system is around 1.5 Gyr; therefore, KIC 6362386 has been synchronized.

To gain a more comprehensive understanding of starspot characteristics, we utilized the depth and duration metrics of starspot signals, along with the single-/double-dip ratio (SDR) as shown in G. Basri & R. Shah (2020), to describe their behaviors. The duration of a starspot corresponds to the time difference between two adjacent minimum values, while the depth signifies the difference between the highest and lowest values of the starspot (J. Wang et al. 2022). Over a rotation period, starspot activity signals typically exhibit one or two minima, referred to as dips. If the duration of a single dip falls between 0.2 and 0.8 rotation periods, it suggests a high likelihood of double starspots on the star (G. Basri & R. Shah 2020). Conversely, the presence of only one starspot within a rotation period is considered when the dip duration exceeds this range. We conducted a statistical analysis of the duration and depth of starspots throughout each rotation cycle, presenting the results in Figure 20. Following the calculation of the ratio of single to double starspots and taking the logarithm, the resulting SDR is −0.49, which indicates that double dips predominantly characterize the starspots in the system.

Table 5
The Independent Frequencies of the Primary Star

Frequency (c/d)	Amplitude (ppm)	SNR
0.16417732	165.33194	28.36
0.18404021	30.25524	5.26

In a study conducted by G. Basri et al. (2022), the relationship between starspot decay timescales and rotation periods was measured using samples from single stars with rotation periods ranging between 3 and 50 days. Upon comparison with their findings, we observed that the decay timescale of 37 days of KIC 6362386 aligns with the trend observed in their study. Furthermore, in comparison with the findings of J. Wang et al. (2022), the decay timescale observed in KIC 6362386 is in line with their conclusions, supporting the notion that the decay timescale of starspots tends to increase with a decrease in rotation period.

In our analysis, we substituted the size of starspots with the rms deviation of the residuals. For KIC 6362386, the starspot size is indicated by rms $= 0.003$, consistent with the observations of J. Wang et al. (2022), who noted an increase in starspot size with decreasing rotation period. Comparing the rms of starspots at the same temperature as reported in H. A. C. Giles et al. (2017), the value for binary KIC 6362386 aligns with their results.

The SDR for KIC 6362386 is calculated at -0.49. In comparison with the binary sample studied by J. Wang et al. (2022), this SDR value is lower than the SDR values for binary stars exhibiting similar decay timescales. This suggests that the starspots in KIC 6362386 tend to manifest in double-dip mode.

4.3. Pulsations

Utilizing the effective temperature and lumination according to the mass and radii values obtained from the modeling of KIC 6362386, we found the primary star is in the instability strip for γ Dor stars as shown in Figure 21. Although the position of the primary star is within the γ Dor pulsating instability strip, the observed characteristics do not align with a typical γ Dor pulsation that has pulsation periods between 0.3 and 3 days (T. Van Reeth et al. 2018). Meanwhile, the secondary star is placed on the main sequence, outside of any instability strip. Consequently, we posit that the variations observed in residuals stem from γ Dor–type pulsations exhibited by the primary star.

After mitigating the effects of starspots, we reanalyzed the frequencies of the residuals with an SNR above 5. Sorting the extracted frequencies in order of amplitude and excluding harmonics and linear combination frequencies, we obtained independent frequencies as listed in Table 5. From the sFT figure as shown in Figure 15, the signal exhibits relative stability, yet some variations in frequency and amplitude persist.

Despite the paucity of frequencies, the stability of the observed frequencies, as evidenced by the sFT, leads us to believe that this star has undergoing stable pulsations. The limited number of frequencies poses a challenge for obtaining additional information, such as period spacing and mode identification.

This finding holds significance for the study of the edges of stellar instability strips and their characteristics. Given the binary nature of the star and the availability of relevant stellar physical parameters obtained through binary modeling, we propose combining the stable pulsation frequencies with the MESA code for model fitting in following work. This will serve as the basis for further research and model simulations on this particular star.

5. Conclusions

We conducted an extensive study on the light curves of the binary system KIC 6362386 from the Kepler and TESS photometry, coupled with RV curves derived through LAMOST spectroscopic observations, allowing the determinations of its orbital and physical parameters for the first time. The primary and secondary stars have masses and radii of $M_1 = 1.43 \pm 0.13\,M_\odot$, $R_1 = 1.68 \pm 0.08\,R_\odot$ and $M_2 = 0.44 \pm 0.18\,M_\odot$, $R_2 = 0.46 \pm 0.06\,R_\odot$, respectively. Additionally, utilizing the Padova isochrone, we determined the age of the binary star to be $1.58^{+0.15}_{-0.13}$ Gyr. By employing the Gaia data, we derived the distance between the binary star and the Sun as 1019 ± 12 pc. Furthermore, upon analyzing the residuals, we identified noticeable signals, for which we investigated potential sources, including surrounding star contamination, starspot signals, and pulsation signals. After ruling out the first two possibilities, we incorporated starspots for fitting due to the asymmetry in the light curve. Subsequently, we determined relevant parameters for the starspots (explained in Section 4.2). The decay time of the starspots is around 37 days and the rotation period is given along with the orbital period because the binary has been synchronized. Considering the effective temperatures of the two components, we believe that the starspots mainly originate from the secondary star, which is an M-type dwarf star. Even after mitigating the influence of starspots, the residual signals persisted. Plotting the primary and secondary stars on the H-R diagram revealed that the primary star lies in the γ Dor instability strip. Although the number of independent frequencies observed is relatively small, the main frequency is 0.1642c/d, which is not a typical frequency of γ Dor–type stars, and we posit that this star has the γ Dor pulsation and undergoing stable pulsations as shown in sFT. The few frequencies and stable pulsations that lead the binary system to be a particular type of star holds significant importance for studying and illustrating the instability strip.

Acknowledgments

J.N.F. acknowledges the support from the National Natural Science Foundation of China (NSFC) through the grants 12090040 and 12090042, and the science research grants from the China Manned Space Project. This research made use of Lightkurve, a Python package for Kepler and TESS data analysis (Lightkurve Collaboration 2018). Guoshoujing Telescope (the Large Sky Area Multi-Object Fiber Spectroscopic Telescope LAMOST) is a National Major Scientific Project built by the Chinese Academy of Sciences. Funding for the project has been provided by the National Development and Reform Commission. LAMOST is operated and managed by the National Astronomical Observatories, Chinese Academy of Sciences. All of the data presented in this paper were obtained from the Mikulski Archive for Space Telescopes (MAST) at the Space Telescope Science Institute. The specific observations analyzed can be accessed via doi:10.17909/3aqh-ah32. STScI is operated by the Association of Universities for

Research in Astronomy, Inc., under NASA contract NAS526555. Support to MAST for these data is provided by the NASA Office of Space Science via grant NAG57584 and by other grants and contracts.

Appendix

This appendix is included to provide a comparison between the light curves obtained through traditional differential photometry and those generated by the LightKurve program. As accurate flux calibration and consistency across data sets are important, this comparison aims to demonstrate the effectiveness and reliability of the differential photometry method. By analyzing both approaches, we seek to highlight potential discrepancies and validate our results, ensuring that our findings on the binary system remain robust and credible. This analysis contributes to the overall understanding of data processing techniques and their impact on astrophysical measurements.

A.1. Differential Photometry

We choose KIC 6362384 (TIC 137088097) and KIC 6362493 (TIC 137088054) as the reference star and the comparison star to do the differential photometry of KIC 6362386. When processing the Kepler and TESS data, we used methods derived from J. Martínez-Palomera et al. (2022) and T. Han & T. D. Brandt (2023), respectively. The final light curves are shown in Figures 22 and 23 for Kepler and TESS data, respectively. To compare the differences between the light curves obtained by the differential photometry and the Lightkurve program, we plotted the results of both methods in a single graph, as shown in Figures 24 and 25. From the figures, we can see that a light curve obtained from differential photometry exhibits greater variability in eclipse depth. Therefore, it is reasonable to use the light curves obtained from the LightKurve program for analysis.

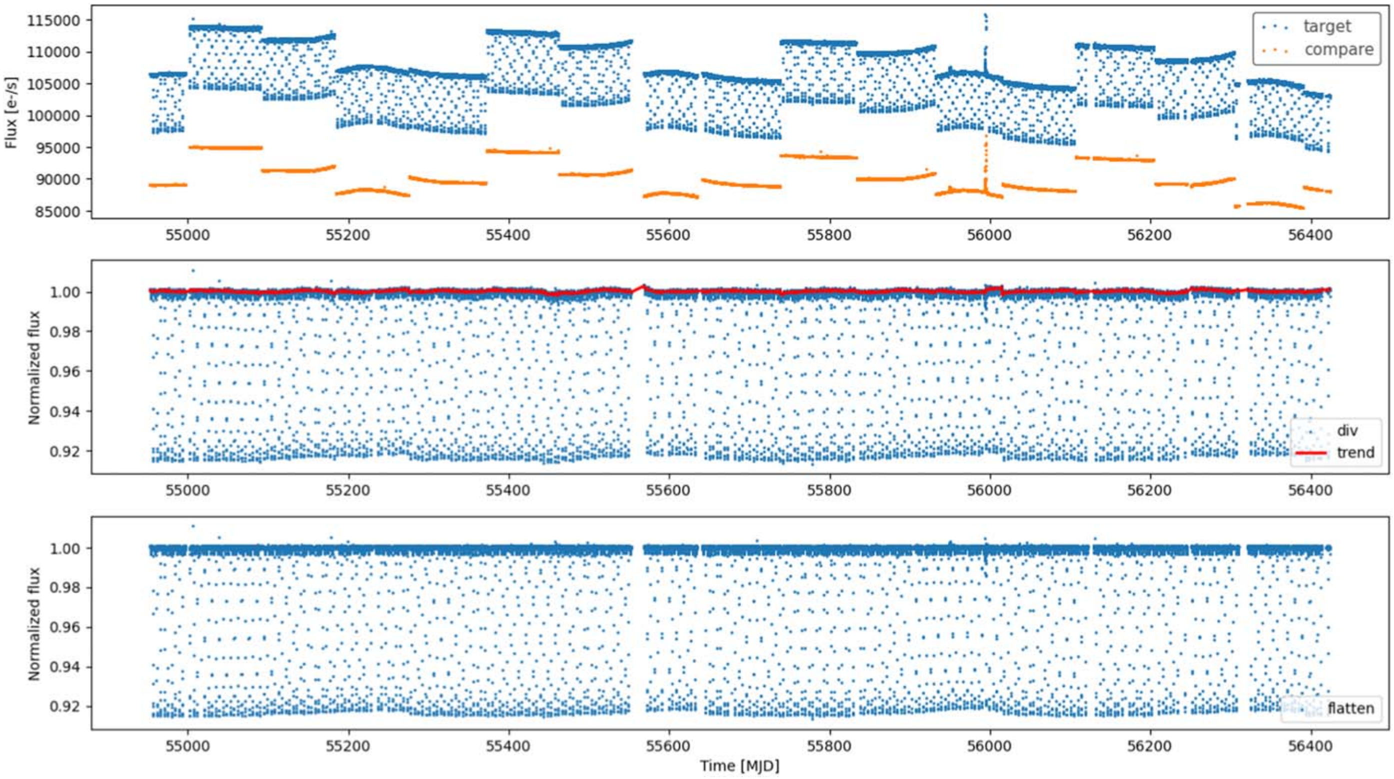

Figure 22. The light curve obtained by differential photometry of the Kepler LC data. The top panel shows the light curves of the target star and the comparison star. The middle panel shows the light curve of differential photometry with the red line indicating the trend of the light curve. The bottom panel shows the detrended light curve of KIC 6362386.

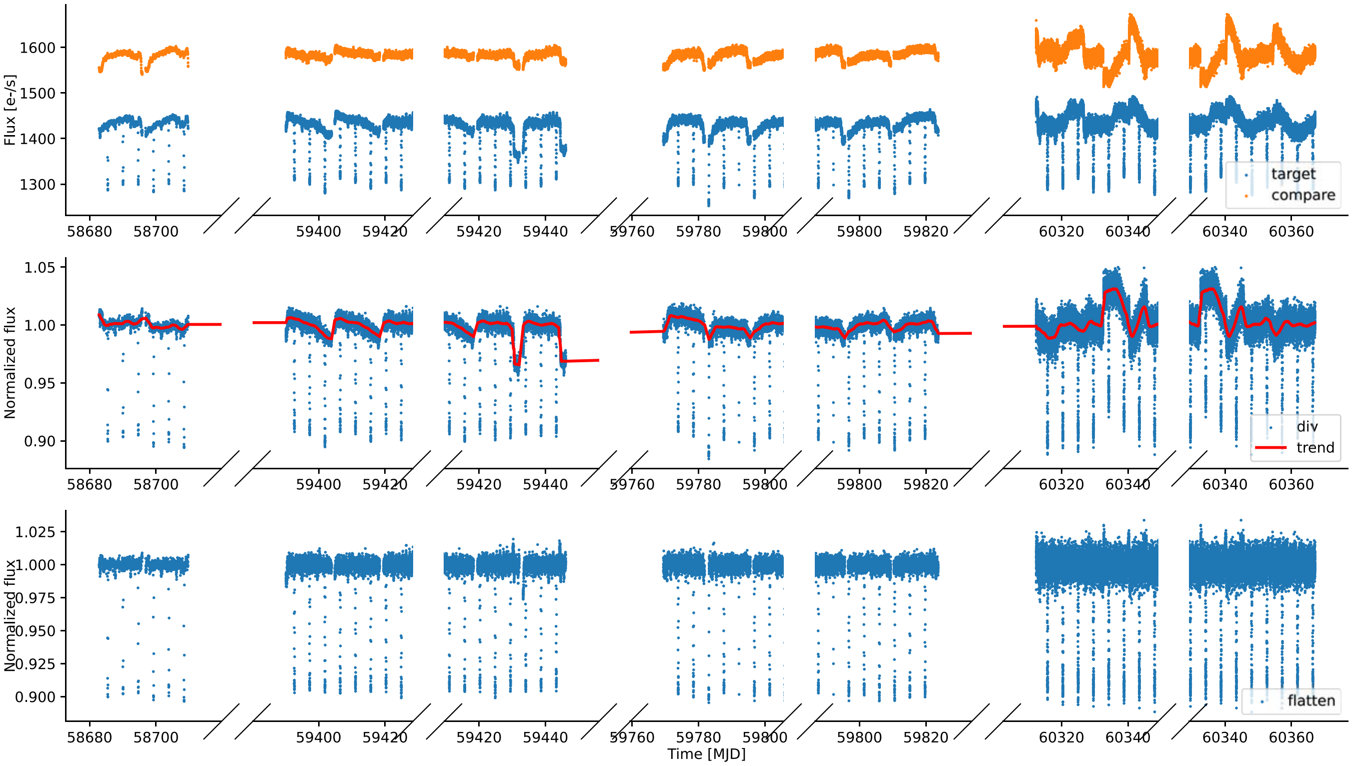

Figure 23. The light curve obtained by differential photometry of the TESS data. The top panel shows the light curves of the target star and the comparison star. The middle panel shows the light curve of differential photometry with the red line indicating the trend of the light curve. The bottom panel shows the detrended light curve of KIC 6362386.

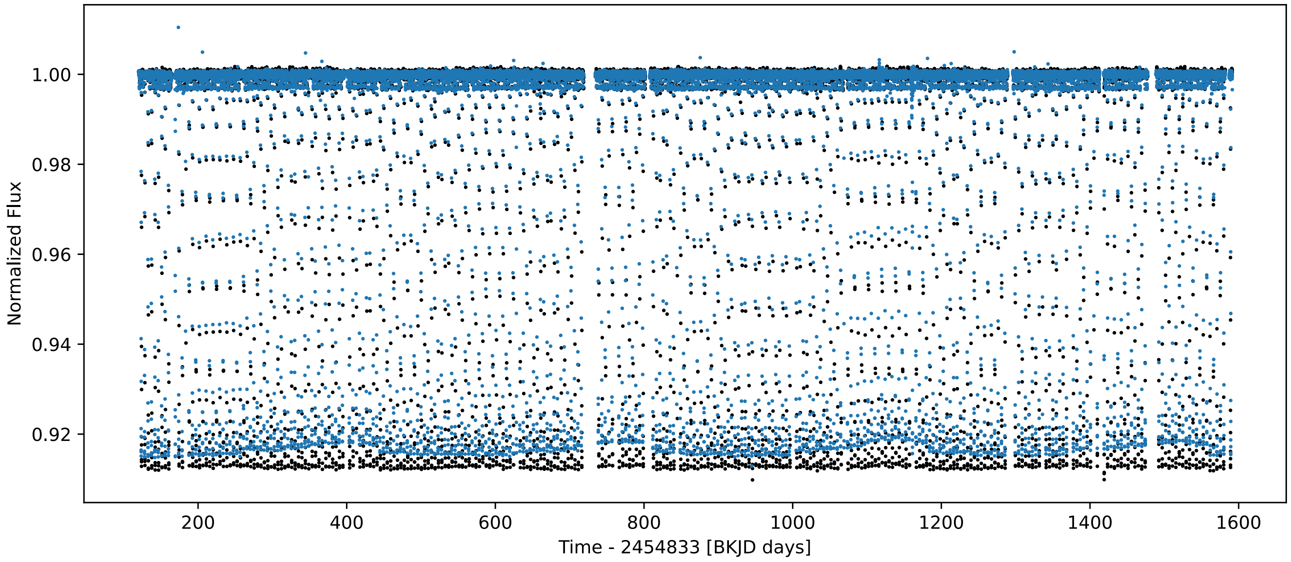

Figure 24. Comparison of the light curves obtained by the LightKurve program and the differential photometry for the Kepler data. The black and blue dots are obtained from the LightKurve program and the differential photometry, respectively.

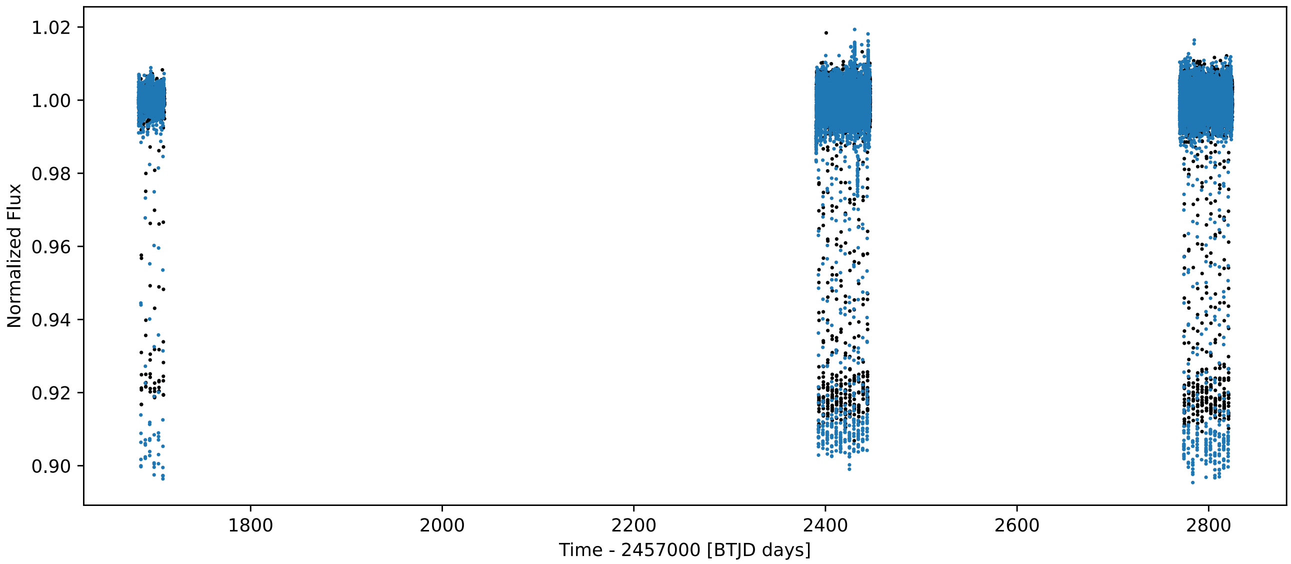

Figure 25. Comparison of the light curves obtained by the LightKurve program and the differential photometry for the TESS data. The black and blue dots are obtained from the LightKurve program and the differential photometry, respectively.

ORCID iDs

Jianning Fu https://orcid.org/0000-0001-8241-1740
Xiaobin Zhang https://orcid.org/0000-0002-5164-3773
Weikai Zong https://orcid.org/0000-0002-7660-9803
Jiaxin Wang https://orcid.org/0000-0002-6868-6809
Xiaoyu Ma https://orcid.org/0000-0002-7468-3612
Keyu Xing https://orcid.org/0009-0003-8858-2833

References

Andrae, R., Fouesneau, M., Creevey, O., et al. 2018, A&A, 616, A8
Angus, R., Morton, T., Aigrain, S., Foreman-Mackey, D., & Rajpaul, V. 2018, MNRAS, 474, 2094
Armstrong, D. J., Pollacco, D., & Santerne, A. 2017, MNRAS, 465, 2634
Bailer-Jones, C. A. L., Rybizki, J., Fouesneau, M., Demleitner, M., & Andrae, R. 2021, AJ, 161, 147
Bailer-Jones, C. A. L., Rybizki, J., Fouesneau, M., Mantelet, G., & Andrae, R. 2018, AJ, 156, 58
Balona, L. A., & Abedigamba, O. P. 2016, MNRAS, 461, 497
Balona, L. A., Krisciunas, K., & Cousins, A. W. J. 1994, MNRAS, 270, 905
Basri, G., & Shah, R. 2020, ApJ, 901, 14
Basri, G., Streichenberger, T., McWard, C., et al. 2022, ApJ, 924, 31
Berdyugina, S. V. 2005, LRSP, 2, 8
Bonanos, A. Z. 2006, in IAU Symp. 240, Binary Stars as Critical Tools & Tests in Contemporary Astrophysics, ed. W. I. Hartkopf, E. F. Guinan, & P. Harmanec (Cambridge: Cambridge Univ. Press), 79
Borucki, W. J., Koch, D., Basri, G., et al. 2010, Sci, 327, 977
Borucki, W. J., Koch, D. G., Basri, G., et al. 2011, ApJ, 728, 117
Bressan, A., Marigo, P., Girardi, L., et al. 2012, MNRAS, 427, 127
Chen, X., Liu, Z., & Han, Z. 2024, PrPNP, 134, 104083
Claret, A., & Bloemen, S. 2011, A&A, 529, A75
Coughlin, J. L., Thompson, S. E., Bryson, S. T., et al. 2014, AJ, 147, 119
Cui, X., Wang, S.-G., Su, D.-Q., et al. 2010, Proc. SPIE, 7733, 77330B
Cui, X.-Q., Zhao, Y.-H., Chu, Y.-Q., et al. 2012, RAA, 12, 1197
De Cat, P., Fu, J. N., Ren, A. B., et al. 2015, ApJS, 220, 19
Dupret, M. A., Grigahcène, A., Garrido, R., Gabriel, M., & Scuflaire, R. 2005, A&A, 435, 927
Foreman-Mackey, D., Conley, A., Meierjurgen Farr, W., et al. 2013, emcee: The MCMC Hammer, Astrophysics Source Code Library, ascl:1303.002
Fu, J., ZONG, W., & WANG, H. 2022, SSPMA, 52, 289502
Gaia Collaboration, Weingrill, K., Mints, A., et al. 2023, A&A, 680, A35
Giles, H. A. C., Collier Cameron, A., & Haywood, R. D. 2017, MNRAS, 472, 1618
Gorynya, N. A., & Tokovinin, A. 2014, MNRAS, 441, 2316
Guo, Z., Gies, D. R., & Matson, R. A. 2017, ApJ, 851, 39
Han, T., & Brandt, T. D. 2023, AJ, 165, 71
Hełminiak, K. G., Moharana, A., Pawar, T., et al. 2021, MNRAS, 508, 5687
Hilditch, R. W. 2001, An Introduction to Close Binary Stars (Cambridge: Cambridge Univ. Press)
Jones, D., Conroy, K. E., Horvat, M., et al. 2020, ApJS, 247, 63
Kaye, A. B., Handler, G., Krisciunas, K., Poretti, E., & Zerbi, F. M. 1999, PASP, 111, 840
Keen, M. A., Bedding, T. R., Murphy, S. J., et al. 2015, MNRAS, 454, 1792
Kirk, B., Conroy, K., Prša, A., et al. 2016, AJ, 151, 68
Kirkpatrick, J. D., Marocco, F., Gelino, C. R., et al. 2024, ApJS, 271, 55
Li, G., Van Reeth, T., Bedding, T. R., et al. 2020, MNRAS, 491, 3586
Lightkurve Collaboration 2018, Lightkurve: Kepler and TESS time series analysis in Python, Astrophysics Source Code Library, ascl:1812.013
Lurie, J. C., Vyhmeister, K., Hawley, S. L., et al. 2017, AJ, 154, 250
Mamajek, E. E., Torres, G., Prsa, A., et al. 2015, arXiv:1510.06262
Martínez-Palomera, J., Hedges, C., Rodriguez, J. E., Barentsen, G., & Dotson, J. 2022, AJ, 163, 93
McQuillan, A., Mazeh, T., & Aigrain, S. 2014, ApJS, 211, 24
Morton, T. D., Bryson, S. T., Coughlin, J. L., et al. 2016, ApJ, 822, 86
Nelder, J. A., & Mead, R. 1965, CompJ, 7, 308
O'Connell, D. J. K. 1951, PRCO, 2, 85
Pan, Y., Fu, J.-N., Zong, W., et al. 2020, ApJ, 905, 67
Pedregosa, F., Varoquaux, G., Gramfort, A., et al. 2011, JMLR, 12, 2825
Prša, A., Batalha, N., Slawson, R. W., et al. 2011, AJ, 141, 83
Prša, A., Conroy, K. E., Horvat, M., et al. 2016, ApJS, 227, 29
Prša, A., & Zwitter, T. 2005, ApJ, 628, 426
Rasmussen, C. E., & Williams, C. K. I. 2006, Gaussian Processes for Machine Learning (Cambridge, MA: MIT Press)
Ricker, G. R., Winn, J. N., Vanderspek, R., et al. 2015, JATIS, 1, 014003
Saio, H., Bedding, T. R., Kurtz, D. W., et al. 2018, MNRAS, 477, 2183
Sekaran, S., Tkachenko, A., Abdul-Masih, M., et al. 2020, A&A, 643, A162
Tonry, J., & Davis, M. 1979, AJ, 84, 1511
Torres, G., Andersen, J., & Giménez, A. 2010, A&ARv, 18, 67
Triana, S. A., Moravveji, E., Pápics, P. I., et al. 2015, ApJ, 810, 16
Van Reeth, T., Johnston, C., Southworth, J., et al. 2023, A&A, 671, A121
Van Reeth, T., Mombarg, J. S. G., Mathis, S., et al. 2018, A&A, 618, A24
Van Reeth, T., Tkachenko, A., & Aerts, C. 2016, A&A, 593, A120
Wang, J., Fu, J., Zong, W., et al. 2022, MNRAS, 511, 2285
Wang, J., Fu, J.-N., Zong, W., et al. 2020, ApJS, 251, 27
Wang, S.-G., Su, D.-Q., Chu, Y.-Q., Cui, X., & Wang, Y.-N. 1996, ApOpt, 35, 5155
Windemuth, D., Agol, E., Ali, A., & Kiefer, F. 2019, MNRAS, 489, 1644
Xing, K., Zong, W., Silvotti, R., et al. 2024, ApJS, 271, 57
Zhang, B., Li, J., Yang, F., et al. 2021, ApJS, 256, 14
Zhang, J., Qian, S.-B., Wu, Y., & Zhou, X. 2019, ApJS, 244, 43
Zhang, X., Chen, X., Zhang, H., Fu, J., & Li, Y. 2020, ApJ, 895, 124
Zhang, X. B., Fu, J. N., Liu, N., Luo, C. Q., & Ren, A. B. 2017, ApJ, 850, 125
Zhang, X. B., Fu, J. N., Luo, C. Q., Ren, A. B., & Yan, Z. Z. 2018, ApJ, 865, 115
Zong, W., Charpinet, S., & Vauclair, G. 2016a, A&A, 594, A46
Zong, W., Charpinet, S., Vauclair, G., Giammichele, N., & Van Grootel, V. 2016b, A&A, 585, A22
Zong, W., Fu, J.-N., De Cat, P., et al. 2020, ApJS, 251, 15